TNO TU Delft

Master Thesis

Space-Based FMCW SAR Systems

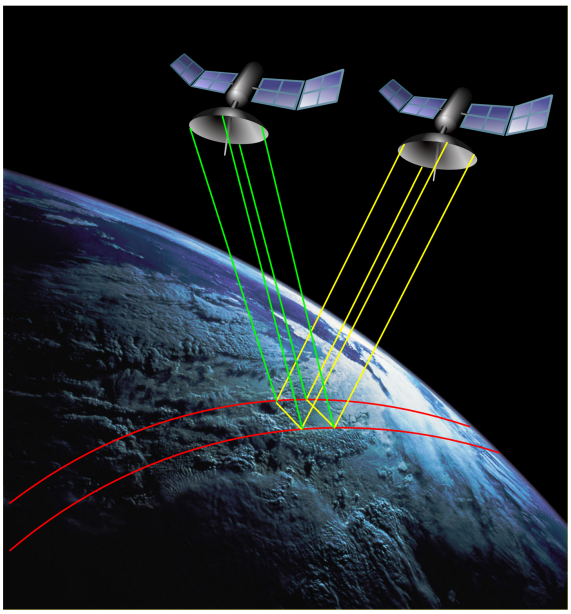

Author:
Maarten van den Oever

Supervisors:
Dr.ir. D. Bekers
Prof.ir. P. Hoogeboom

August 31, 2012

Contents

Abstract

Monitoring critical structures such as oil pipe lines or dikes is essential for performing in-time and high-quality maintenance. Such structures cover a large area or are in abandoned places. Consequently, performing physical inspections by dedicated personnel is either impossible or very expensive. Alternatively such structures can be inspected by using satellite radar data. Synthetic Aperture Radar (SAR) data is already being used to create images of large areas. However, the current satellite SAR systems are big and require a lot of power, which makes their data expensive. In the TOFsat project the feasibility of a lightweight and low power FMCW SAR instrument for space is investigated. This work is part of the feasibility study.

In the analysis of the power budget multiple feasible combinations for transmit power and antenna size where discussed, the preferred option is a option with 50 dBW transmit power and 6.25 m^2 antenna area. In our configuration of the radar ambiguities are present.

The ambiguous projection of the ground directly under the satellite, called the nadir return, can distort the final image. However by carefully selecting the pulse repetition frequency the projection can be shifted outside the image of the area of interest.

The utilization of FMCW on a SAR satellite introduces high demands on the isolation between the transmit chain and the receive chain. A single antenna solution on a single satellite with a circulator can not provide the required isolation. To avoid this problem a gating scheme was proposed. However a space based implementation of a gating scheme resulted in conflicting values of the gating frequency and pulse repetition frequency. Therefore gated FMCW did not resulted in a feasible solution. Having two separate antennas increases the isolation between the transmit chain and the receive chain. However from phase noise calculations it followed that still 100 dB of isolation was required. These high values of isolation are still difficult to obtain, together with the fact that two antennas on one satellite would have been required this led to a preference for a bi-static system.

For a more accurate simulation of the system performance the far field antenna pattern was required. Multiple antenna options where considered, based on weight efficiency the slotted waveguide array was selected for this project.

The available simulation tools within TNO did not take into account the mutual coupling of the slots of the array. To find the far field pattern first the slot voltages needed to be known. To compute the slot voltages a linear system of equations has been generated. After applying corrections to make the expressions convergent, a tool has been generated. With the obtained slot voltages the far field pattern can be generated. Resulting in a tool that is capable of simulating the far field pattern of a slotted waveguide array.

Acknowledgements

I would like to thank TNO for giving me the opportunity to work on the TOFsat project, participate in the CDF sessions, and attend the ARSI workshop which all gave me the possibility to learn a lot of new things. Also I would like express my gratitude to Sefania Monni and Matern Otten for their technical support. I specially would like to thank Dave Bekers and Peter Hoogeboom for their technical and non-technical support during my thesis. Furthermore I would like to thank all other employees of TNO that made my stay with TNO pleasant. Finally I would like to thank my friends and family for their support.

Maarten van den Oever
Delft, The Netherlands
August 31, 2012

Chapter 1

Introduction

This chapter starts with the motivation for the design of a space based FMCW SAR system. Then the TOFsat project is introduced. Next the aim of this thesis is presented. In the last part of this section the content of this report is presented.

1.1 Motivation

Monitoring critical structures such as oil pipe lines or dikes is essential for performing in-time and high-quality maintenance. Such structures cover a large area or are in abandoned places. Consequently, performing physical inspections by dedicated personnel is either impossible or very expensive. Alternatively such structures can be inspected by using satellite radar data. Synthetic Aperture Radar (SAR) data is already being used to create images of large areas. However, the current satellite SAR systems are big and require a lot of power. This makes the existing systems expensive to develop and manufacture. Moreover there is limited availability of data, i.e. the time between successive passes is large. This makes the cost of the data high and thus creates a barrier for the usage of the data.

To make the usage of SAR data interesting for smaller projects, the cost of the data needs to be lower while maintaining sufficient quality. This can be achieved by the usage of Frequency Modulation Continuous Wave radar techniques (FMCW). FMCW is a technique that has low peak powers due to the continuous operation. This leads to higher efficiency compared to systems where there is an instant demand of high peak powers. An FMCW radar has a simpler design than a conventional radar. Therefore it is smaller and lighter than a conventional pulsed radar system, this makes it cheaper to launch. Since FMCW operates continuously, the transmission of the signal occurs at the same time as the reception of the returned signal. This poses high demands on the isolation between the transmit chain and the receive chain. In space systems the transmit power needs to be higher than in earth systems. Accordingly the measures for isolation between the transmit chain and the receive chain need to be increased.

In this thesis we study specific issues in the design and development of a small FMCW SAR radar for earth monitoring. Our study is related to the so-called TOFsat project, a Netherlands Space Organisation (NSO) PEP project carried out by TNO and the SME SSBV.

1.2 TOFsat Project

The TOFsat project has been set up to study the feasibility of a small satellite to gather SAR data at low cost. Data of such a satellite can be used for several applications like ground imaging, dike monitoring, and oil pipeline monitoring. For such applications a ground range resolution of about $4 - 6$ meter at X-band is required. The required width of the imaged strip, the swath, is not specified. However the larger the swath width the better, with a wider swath less passes are required to image a certain area. The requirements on the ground range resolution and swath

width of the TOFsat satellite are not revolutionary, the requirements on size, weight and cost make the TOFsat project unique. Satellites with the same or better capabilities, as specified in the project are already in space. However the existing systems are bigger, weigh more and are more expensive to build, which results in more expensive data. Due to the demand for relatively low cost data some strict requirements on size and weight are posed. A satellite with a weight of about 150 kg and dimensions smaller then 1 m^3 can be launched as secondary payload, which helps to keep the costs low. The initial design parameters that follow from the desire to be launched as secondary payload make the TOFsat project revolutionary.

One of the satellites that is already in use is the commercial SAR satellite TerraSAR-X [1] [2]. The radar of TerraSAR-X operates in X-band, it can achieve a resolution of about 1 m in azimuth and 1 m in ground range. This resolution is obtained if one patch is illuminated for a longer period than in conventional SAR, this is done using beam steering. In a conventional SAR configuration the resolution is 3 m in azimuth and up to 3 m in ground range, with a swath width of 30 km. The mass of the satellite is over 1000 kg and the power delivered by the solar panels is 800 W.

The TerraSAR-X satellite has slotted waveguide antennas. The antennas are 40 cm long each and fed from the centre, the width is not specified. The satellite is covered with 4 panels consisting of 3×32 arrays each. The total antenna area is 4.8 m $\times$ 0.75 m. The slotted waveguide antennas are specially designed to enable both horizontal and vertical polarisation.

Another SAR satellite that is already in space is the TecSAR satellite [3]. TecSAR is a Israeli military surveillance satellite. The TecSAR has a similar as high resolution mode as TerraSAR-X. In TecSAR also a resolution of 1 m in range and azimuth is obtained in this mode. The regular SAR resolution is 3 m in azimuth and 3 m in ground range. The satellites mass is about 300 kg. TecSAR uses a parabolic dish as an antenna. The feed of that antenna has multiple transmitters and receivers to perform beam steering. To extend the scanning capabilities the satellite is capable of mechanical steering. With the added scanning capabilities a fast scanning mode is created with narrow overlapping beams capable of obtaining an azimuth resolution of 1.8 m. The swath width is not exactly specified however there is stated that using a low resolution a swath of 100 km can be imaged.

In our satellite the space for the folded antennas and solar panels is limited, due to the small volume. This will limit the total size of the solar panels and antennas. This will have a large impact on the performance of the final radar system. The small solar cells will pose restrictions on the power consumption by the satellite bus and SAR instrument. The limited antenna dimensions will affect the radar performance.

In two Concurrent Design Facility sessions the global design of the satellite was discussed. The teams consisted of engineers of TNO and SSBV in satellite engieneering and radar engineering. During these sessions various satellite configurations, with different antenna dimensions and different power budgets where investigated. The different configurations with their corresponding available antenna areas where used in this report.

1.3 Aim of the Thesis

Space based operation of an FMCW radar system presents additional challenges on the system design compared to airborne operation. Due to the height of the satellite and the large distance to the swath the return power from the radar is low compared to the transmitted power and the received noise, which poses high demands on the isolation. The large distances from the satellite to the swath, result in the swath being located at multiple times the ambiguous range of the radar. This can cause ambiguous projections to be imaged in the swath.

The aim of the thesis is to support the design team of TNO at system level by investigating specific topics regarding system performance, like power budget and range ambiguities, and data downlink. The second part of this thesis focuses on the development of a code for rapid evaluation of a single slotted waveguide antenna. This code has to result far field patterns with the mutual coupling of the slots included.

1.4 Contents of the Thesis

This report consists of 6 chapters. In Chapter 2 we are going to introduce the SAR principles and the FMCW technique. After this the range ambiguities are going to be discussed and the concepts of mono-static systems and multi-static systems are going to be introduced.

In Chapter 3 the system aspects regarding the radar operation and the hardware of the radar system are going to be addressed. In Chapter 3.1 the power budget and the Noise equivalent sigma zero for a feasible system are going to be investigated. The range ambiguities are going to be extended with the nadir return in Chapter 3.2. The additional requirements regarding the isolation when using FMCW and their impact on the system configuration are going to be addressed in Chapter 3.3.

For the final system model the antenna needs to be selected. The impact of the antenna selection is more than the difference in gain of a certain antenna type. The choice of the antenna also has impact on the weight of the satellite, the shape of the satellite, the power required by the satellite, and the electronics that can be used to excite the antenna. The antenna selection and description of the general impact is presented in Chapter 3.4. When a radar has gathered its data it has to be sent to the ground. In FMCW SAR a large amount of data is gathered due to the continuous sampling. One of the requirements on the downlink is the ability of downlinking the data in real-time. Also the downlink should be compatible to work with existing ground stations. A downlink capable of downloading the data in real-time has to be designed, this is presented in Chapter 3.5.

To evaluate the effects of the antenna selection, the antenna needs to be modelled. For a slotted waveguide antenna the simulation using conventional EM solvers takes a lot of computational time. To enable rapid prototyping of waveguide designs a model needs to be derived. The numerical model that is derived is a first step for later full 3D analysis of the slotted waveguide problem.

In Chapter 4 the mathematical model of the slotted waveguide is going to be derived. The model that is derived is implemented in Matlab, as described in Chapter 5. The Matlab codes are validated with test cases from literature. And in the last chapter the conclusions and recommendations of the thesis work are going to be presented.

Chapter 2

Synthetic Aperture Radar

The concept of Synthetic Aperture Radar (SAR) has been developed in the 1950s. Due to the high requirements on the processing it did not immediately become successful. After the introduction of the FFT algorithm and the increase of computational power the usage of SAR became more popular. SAR is utilised in remote sensing applications and land monitoring. The radars used for SAR are often mounted on air planes or satellites.

In this chapter first the concepts behind SAR are going to be explained. Then the concept of Frequency Modulated Continuous Wave (FMCW) radar and the utilisation of FMCW for SAR are going to be discussed. In the last section mono-static and multi-static platforms and their advantages and disadvantages for usage with an FMCW radar system are going to be explained.

2.1 SAR Principles

Synthetic Aperture Radar (SAR) is a remote sensing technique that is used to obtain high precision imaging data. SAR uses the movement of the platform to emulate a large antenna array. The large antenna is emulated by taking measurements at different points along the flight path. In a typical SAR system the antenna is side-looking. The geometry of such a system is given in Figure 2.1.

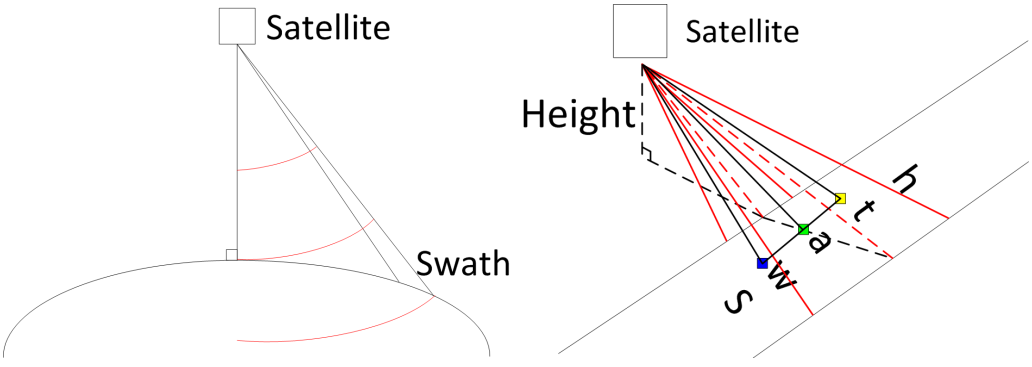

Figure 2.1: Geometry of a spaceborne SAR sensor

In Figure 2.1 a platform equipped with a SAR radar is moving parallel to a strip of ground. That strip of ground is called the swath. The antenna mounted on the platform is pointing to the swath and thereby illuminating a part of the swath. By moving parallel to the swath the total swath is imaged. Seen from the radar a target enters the beam at a certain point, illustrated by

the blue square in Figure 2.1b. Then for the radar the target moves closer towards the radar until it arrives at the centre of the beam, illustrated by the green square. Moving away from the centre of the beam the target also moves away from the radar illustrated by the yellow square. For the radar this change of distance appears as a phase shift that is symmetric around the centre of the beam. Due to the described changes in the targets distance to the radar the Doppler frequency also changes from positive to negative. A representation of the phase history and Doppler history is shown in Figure 2.2. Every location within the swath that is going to be imaged has its own

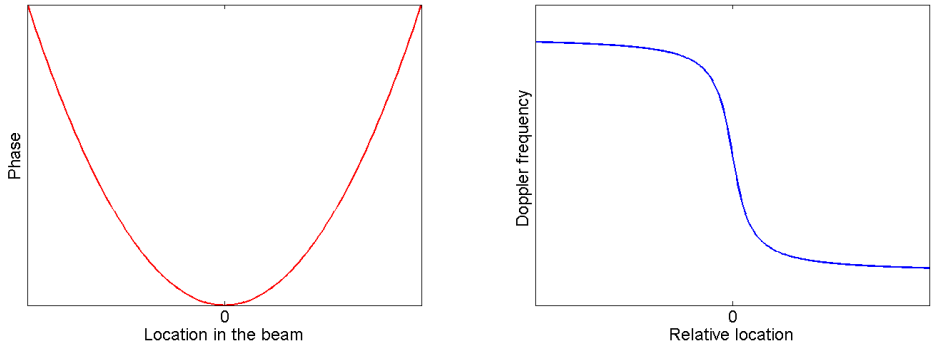

(a) (b)

Figure 2.2: Graphical representation of the unwrapped phase(a) and Doppler(b) history of a target.

phase history and Doppler history. The function of the phase history can be used to identify the power that has returned from a certain location. This is done by correlating the obtained data with reference phase history functions. The steps involved with the signal processing are outside the scope of this work, more information about the signal processing can be found in [4].

Due to the movement of the platform in conventional SAR a 2D image of the ground can be generated. The final image will have a resolution in both dimensions. The resolution in range in conventional radar is given by,

$$\Delta R = \frac{c}{2B}\,, \tag{2.1}$$

where ΔR is the range resolution, c the speed of light and B the bandwidth. In SAR this range resolution is also called the slant range resolution. However the swath is imaged under an angle, as can be seen in Figure 2.1. The resulting resolution of the imaged swath is called the ground range resolution. The difference between the resolution and the ground range resolution is shown in Figure 2.3. The ground range resolution is given by,

$$\Delta R_g = \frac{\Delta R}{\sin\theta_{inc}}\,, \tag{2.2}$$

where θ_{inc} is the incidence angle with the earth.

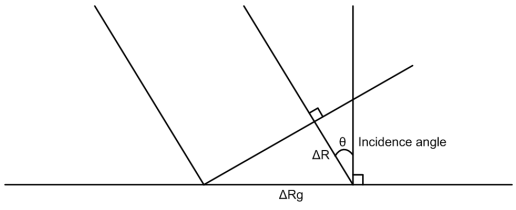

Figure 2.3: Range resolution in SAR

The maximum resolution for a SAR radar in the flight direction, called the azimuth resolution, is half the antenna length in flight direction. This can be derived with the approximate formula for the beam width, β,

$$\beta = \frac{\lambda}{L}\,, \tag{2.3}$$

where λ is the wavelength and L the length of the antenna in the azimuth direction. If this formula is multiplied with the distance to the swath (H) the footprint of the antenna in azimuth direction is obtained, $L_{synth} = \frac{\lambda H}{L}$. This footprint is also the effective length of the synthetic aperture, i.e. the length of the flight path where a certain point of the swath is in the radar beam. This length can be used to calculate the beam width of the synthetic antenna, which is given by,

$$\beta_{synth} = \frac{L}{H} \tag{2.4}$$

This effective beam width of the synthetic aperture can now be used to calculate the length of the footprint of the synthetic antenna in azimuth direction. This is done by multiplication with the distance to the swath. The footprint becomes L, the original antenna length. The missing factor two can be found in the difference in amplitude response pattern of the antenna and the synthetic antenna, which is explained in [5, Ch. 9.6.1].

To obtain this azimuth resolution at least two pulses per antenna length need to be transmitted to obey the Nyquist criterion. This leads to a high pulse repetition frequency since the speed of the satellite is high and thus the time between samples is short. The minimum pulse repetition frequency follows directly from the velocity of the satellite and is given by,

$$PRF_{min} = \frac{2V}{L}\,, \tag{2.5}$$

where V is the velocity of the satellite. This formula shows the direct relation between the velocity of the satellite and the minimum pulse repetition frequency. The velocity of a satellite to maintain its orbit can be calculated using formula found in [6] and [5, Ch. 10.3], given by,

$$V_{orbit} = \sqrt{\frac{GM}{R}}\,, \tag{2.6}$$

where R is the radius of the orbit, constants G and M represent the earth's gravitational field and the earth's mass. For an example satellite system with an altitude of 600 km and an antenna with the length 4 m in the direction of the flight path the minimum PRF is calculated resulting in the parameters in Table 2.1 .

Table 2.1: Parameters of an example satellite

Variable	Value
Altitude	600 km
Radius of the earth	6400 km
Radius of the orbit (R)	7000 km
Antenna length (l)	4 m
Earth's gravitational field (G)	$6.6726 \cdot 10^{-11}$ N m^2 kg^{-2}
Earth's mass (M)	$5.972 \cdot 10^{24}$ kg
Satellite's velocity V	7545 m/s
Minimum PRF	3.8 kHz

The minimum PRF for this system is 3.8 kHz, a different orbit would result in a different orbit speed and a different PRF. However the selection of the final PRF should also depend of the range ambiguities that are present. The range ambiguities are discussed in Chapter 2.3.

2.2 FMCW

Frequency Modulated Continuous Wave (FMCW) radar is a radar technique that continuously transmits a low power signal. This is different from conventional pulsed radar systems, where only short high power pulses are transmitted. In FMCW the transmitted frequency is increased over time during one sweep time. After the sweep time the system returns to the frequency where the previous sweep started and starts again, this is called a sweep. This process is repeated continuously. The Sweep Repetition Frequency (SRF) is defined as one divided by the time of the sweep(T_s), $\frac{1}{T_s}$. Figure 2.4 shows the waveform of an FMCW Signal. The signal that is received is mixed down with the transmitted signal. If a target is present its reflection is measured at the radar as a frequency difference between the transmitted signal and the received signal. The frequency corresponding with the difference is called the beat frequency and it can be used to obtain the distance of the target.

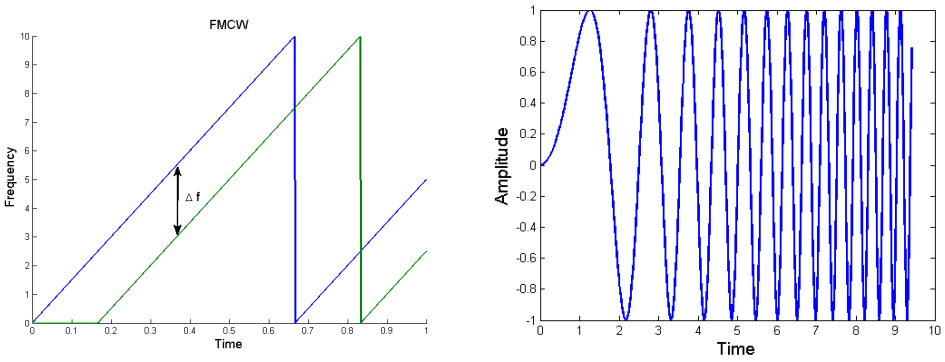

(a) (b)

Figure 2.4: The FMCW waveform.

FMCW radar can be used to perform SAR. The implementation of FMCW for SAR is not trivial. SAR performed with a pulsed radar depends on the stop and go principle, the platform can be assumed stationary during the transmission of the short pulse. Since in FMCW the transmission of the signal is continuous, this approximation is not valid. In [7, Ch. 4] the effects of the movement of the platform are investigated. The conclusion is that the effect of the platform movement can be compensated in FMCW by applying an additional phase term in the processing.

An example of an existing FMCW SAR system is described in [8]. In this system an FMCW radar was mounted on a small air plane. The radar operates in X-band and has a transmitted power of 63 mW. The geometry in the system is not presented in the paper. In [9] the same platform is used with altitudes of 100 m - 300 m.

In present space applications, SAR is only performed with pulsed radar systems. Due to the increase of processing power and electronics with more capabilities, FMCW becomes feasible for space applications. The advantages of the use of FMCW are lower transmitting power and simpler system design. Both advantages make the FMCW radar suitable for usage in a small satellite. A disadvantage of FMCW radar is the demand for high isolation between the transmitter and receiver due to the continuous transmission of the signal.

2.3 Range Ambiguities

In an FMCW radar system range ambiguities may occur, the effect of that ambiguity is depending on the design of the system. The ambiguity in range is caused by the frequency of the continuous repeating sweeps. A returned signal of a target can arrive after the end of the sweep it originated. This returned signal will now be mixed down with another sweep than it originated from. As a

result it will look like the returned signal originated from a sweep that was transmitted later and the target will appear closer than it really is, this is illustrated in Figure 2.5. In Figure 2.5 an

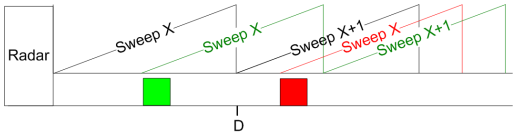

Figure 2.5: Illustration of ambiguity

FMCW radar system is shown that starts transmitting at sweep X. In this sweep the situation is as desired, the green target is imaged at its proper location. Now if the system is transmitting the second sweep, X+1, first the reflection of the red target from sweep X will arrive before the reflection of the green target from sweep x+1. Thus the red target will be imaged before the green target. Since the FMCW is a continuous process, this effect will be present for any ambiguous detection. Thus the reflection that is received at a given moment can originate from any of the previously transmitted sweeps. The location of the target is now described by the frequency difference between the transmitted and the received sweep plus a number of times the distance that one sweep can uniquely identify. The two way distance travelled by the radar wave during one sweep is called the unambiguous range and is given in formula form by,

$$D = \frac{c}{2\mathrm{SRF}}\,, \tag{2.7}$$

where D is the unambiguous range, c the speed of light and, SRF the sweep repetition frequency. In satellite systems the unambiguous range is shorter than the range to the swath. This is an effect of a high sweep repetition frequency and the long distance between the radar and the swath. As an effect ambiguous projections of the earth may be present, especially nadir return and strong reflections from objects at larger distances than the swath. The nadir return is the return from the perpendicular projection on the earth. The mirror like reflection from the earth has the least range attenuation and should be considered in the design. The nadir return is discussed in Chapter 3.2. All the ambiguous projections are in general seen via the side lobes of the antenna pattern. By carefully designing the antenna they can be suppressed to acceptable levels.

2.4 Mono-static / Multi-static

Most pulsed radar systems in space are mono-static, this means that the transmitting antenna and the receiving antenna are co-located. If the transmitting antenna and the receiving antennas are not co-located, for example on different platforms, the configuration is called bi-static or multi-static. Multi-static configuration of a radar can have advantages in certain applications. When in multi-static operation more then one receiving antenna is pointed to the swath interferometric measurements can be performed.

When the radar is an FMCW radar the creation of a mono-static system for a small satellite is difficult. FMCW radar requires high isolation between the transmit chain and receive chain. In a configuration with one satellite that is carrying both the transmitter and receiver it is hard to obtain sufficient isolation. Therefore a mono-static FMCW system for space is difficult to achieve. Calculations to find the required isolation for a space based FMCW radar are presented in Chapter 3.3.

When the transmitter and receiver are placed at different platforms, i.e. a multi-static configuration, the isolation between the transmit chain and the receive chain is not an issue. Another advantage in the case of multi-static operation is the power that has to be delivered by the solar panels. For small satellites it is an issue to generate sufficient power, since the space for solar panels is limited. By separating the transmitter and receiver over two satellites the required power per satellite is reduced. However the multi-static operation causes more difficult processing and complex synchronisation. Also the costs of the launch of an extra satellite are a disadvantage.

Overall multi-static operation with more than one receiving antenna pointing to the swath results in obtaining interferometric data instantly. However if the system only has one transmitter and one receiver on two satellites this advantage is not present. A mono-static system is more cost effective than such a configuration. However the isolation between the transmit and receive chain is an issue. The analysis of the extra costs, benefits, and the technical analysis of the synchronisation of multi-static operation are not addressed in this work. All aspects concerning the satellite and system configuration where discussed and analysed in great detail in the concurrent design team that investigated the feasibility of a small satellite FMCW SAR. The requirements on the isolation between the transmit chain and receive chain are discussed in Chapter 3.3.

Chapter 3

System Aspects

In Chapter 2 the concept of FMCW SAR was introduced. To create a satellite SAR system this concept and its limitations needs to be translated to system requirements. In this chapter we present trade-off's that need to be made for the design of the final system. First the noise equivalent sigma zero and the power budget are going to be investigated in Chapter 3.1. The range ambiguities with a focus on the nadir return are going to be addressed in Chapter 3.2. Then system configurations for some mono-static configurations and a bi-static configuration are going to be presented in Chapter 3.3. The antenna options and their impact on the system are going to be evaluated in Chapter 3.4. Finally the downlink is discussed in Chapter 3.5.

3.1 NESZ and Power Budget

The Noise Equivalent Sigma Zero (NESZ) is one of the principal specifications on the SAR instrument. It is a measure for the sensitivity of the instrument and is defined as the value of the surface scattering coefficient σ_0 that is obtained if the signal power equals the system noise. The NESZ is derived from the radar equation,

$$P_r = \frac{P_t G_t G_r \lambda^2 \sigma}{(4\pi)^3 R^4 L_s}\,, \tag{3.1}$$

where P_r is the received power, P_t is the transmitted power, G_r is the receive antenna gain, G_t is the transmit antenna gain, σ is the radar cross section of the target, and L_s are the system losses. In the TOFsat SAR system the transmit and receive antenna have the same gain, $G = G_t = G_r$, which can be computed by

$$G = \frac{4\pi A_e}{\lambda^2}\,, \tag{3.2}$$

where A_e is the effective antenna area, which consists of the physical area multiplied with an efficiency factor. For SAR applications the surface scattering of the ground is the required property, in normal radar systems this is often called clutter. Thus σ is replaced by the received power from one range bin, given by the range R times the beam width in azimuth θ_{az} times the ground range resolution ΔR_g times the σ_0. To obtain the Clutter to Noise Ratio (CNR) at the receiver the noise needs to be known. The noise that is present is given by, $N = TkBF$, where T is the noise temperature, k is the constant of Boltzmann, B is the bandwidth of the signal and, F the noise factor of the system. The equation for the clutter-to-noise ratio becomes,

$$\mathrm{CNR} = \frac{P_t G^2 \lambda^2 \theta_{az} \Delta R_g \sigma_0}{(4\pi R)^3 k T B F L_s}\,, \tag{3.3}$$

In [10] the expression of the CNR for an FMCW SAR system is given. It is given by,

$$\mathrm{CNR}_{SAR} = \mathrm{CNR} \cdot \frac{\lambda \mathrm{SRF}}{2V\theta_{az}}\,, \tag{3.4}$$

where V is the speed of the platform. For SAR systems the noise bandwidth after SAR processing bandwidth is approximately the SRF. If the clutter-to noise ratio is set to one and the sigma zero is brought to the other side of the equation, on the left side a value is obtained that represents the sigma zero value that can be seen with a CNR of 1. The NESZ is given by $\frac{\sigma_0}{\mathrm{CNR}}$[11], [10] and its expression is given by,

$$\mathrm{NESZ} = \frac{2(4\pi R)^3 kTFL_sV}{P_tG^2\lambda^3\Delta R_g}\,. \tag{3.5}$$

The NESZ for the system is specified as less than -18 dB over the swath. Equation (3.5) shows that the NESZ depends on the noise, the orbit, the transmit power, the antenna gain, and the ground-range resolution. The main design parameters in the system are the transmit power and the antenna gain, which is determined by the antenna size. The platform speed and orbit, thus height and range, are defined in the project. The ground-range resolution has to be as small as possible to have a business case for the project. The losses and noise temperature are determined by the receiver hardware. The largest antenna that could be mounted on one small satellite has a length of about 3 meters. To investigate the feasibility of the system some options have been simulated. To perform this simulation a code has been generated by M. Otten. This code is capable of calculating the NESZ over the swath for a satellite with an antenna with a sinc^2 far field pattern. The program also can calculate the impact of some ambiguous projections that are present, this is discussed in Chapter 3.2. However they use the sinc^2 far field pattern which might not always be correct. In the simulations the isolation between transmit and receive is assumed to be infinite. To meet this requirement in practice the system needs to be bi-static or transmission needs to be stopped while receiving.

The options that are simulated represented by their antenna size and are:

- 3×1 meter antenna
- 2×2.5 meter antenna
- 2.5×2.5 meter antenna

The simulations of the NESZ for these options are presented in Figure 3.1. The simulations are run for a maximum incidence angle of 24°. This corresponds to range from the satellite to the intersection of the beam with the ground of about 645 km. This is equivalent to a ground range of roughly 235 km to the perpendicular projection of the satellite with the earth. For clarification refer to Figure 2.1 for the geometry of the system. For the far field antenna pattern, in these simulations a sinc^2 far field pattern is assumed.

Table 3.1: System parameters of a SAR instrument, the antenna efficiency, the additional loss, and the noise figure are estimates.

Variable	Value
Transmit power	100 W
Antenna size	3 m^2
Antenna gain	44.5 dB
Azimuth beam width	0.0105 rad
Elevation beam width	0.0316 rad
Incidence angle	24°
Antenna efficiency	70 %
Additional loss	3 dB
Noise figure	3 dB
Sweep B	40MHz
SRF	5120 Hz
Swath width	8 km

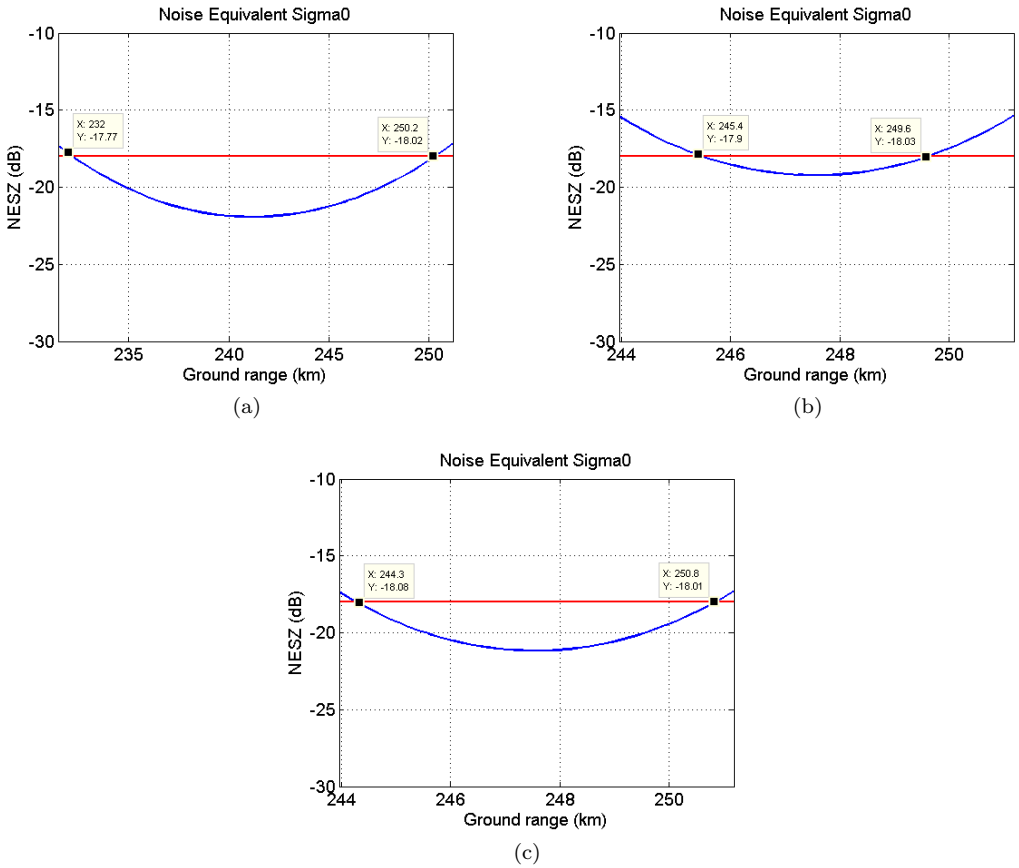

Figure 3.1: NESZ as function of the ground range for three different designs. (a) 3 m^2 antenna with 100W transmit power and 10 meter resolution. (b) 5 m^2 antenna with 50 W transmit power and 4 meter resolution. (c) 6.25 m^2 antenna with 50 W transmit power and 4 meter resolution.

The first simulation is shown in Figure(3.1a). It shows the simulation for a configuration with an antenna surface of 3 m $\times$ 1 m, the length is parallel to the flight path. The parameters of this system are presented in Table 3.1. The transmitted power is 100 Watt and the ground-range resolution is 10 meters. In the presented figure for this configuration the red line indicates the NESZ of -18dB. The area where the NEZS is under -18 dB is 231 km ground range until 250 km ground range. This is sufficiently large to accommodate the swath, thus a feasible system is possible with these parameters. However the 10 meters ground-range resolution might not be sufficient from a commercial point of view.

Another configuration that is considered is a satellite with an antenna with a length of 2 meters in the direction of the flight path and a width of 2.5 meters. In Table 3.2 the changed parameters compared to the previous example are shown.

In this example the sweep repetition frequency has increased to 8 kHz. This is due to the shorter length of the antenna in azimuth direction. Also the transmit power is lowered to 50 W, this is possible due to the larger antenna area which provides more gain. The increased bandwidth makes a ground-range resolution of 4 meters possible. This leads to a NESZ as in Figure (3.1b). The swath of 3 km can be accommodated in the area where the NESZ is below -18 dB, roughly 245.5 km ground range until 249.5 km ground range. Thus a high resolution option is possible.

The last option is to use an antenna with a maximum length of 2.5 meters and a width of 2.5 meters with 50 Watt transmit power and 4 meters ground-range of which the parameters are shown in Table 3.3. In this option the antenna is slightly longer in azimuth direction which gives

Table 3.2: Changed system parameters of a SAR instrument, for a radar with an antenna of 2 meters times 2.5 meters

Variable	Value
Transmit power	50 W
Antenna size	5 m^2
Antenna gain	46.5 dB
Azimuth beam width	0.0156 rad
Elevation beam width	0.0105 rad
Sweep B	100MHz
SRF	8000 Hz

Table 3.3: Changed system parameters of a SAR instrument, for a radar with an antenna of 2.5 meters times 2.5 meters

Variable	Value
Transmit power	50 W
Antenna size	6.25 m^2
Antenna gain	47.5 dB
Azimuth beam width	0.0105 rad
Elevation beam width	0.0105 rad
Sweep B	100 MHz
SRF	6220 Hz

the possibility to lower the SRF compared to the previous example. The antenna area has also increased leading to a higher gain. In the simulations this leads to a lower value of the NESZ. The simulations for this option are shown in Figure(3.1c). Since the NESZ is less than -18 dB for an area ranging from 244 km ground range to 250 km ground range, which is larger than the swath of 3 km, the option results in a feasible system.

From these examples can be concluded that a small SAR system with a ground range resolution of 4 meters can be made. However in these simulations the requirements for isolation between the transmit chain and receive chain in FMCW have not been addressed. Also ambiguous projection from the nadir might be an issue.

3.2 Nadir Return

In Chapter 2.3 range ambiguities where introduced. The consequences of these ambiguities depend on the system parameters. By changing the system parameters the effects in the final radar image can be identified and suppressed or be avoided. For some concepts the system characteristics will be explored in this section. In the system evaluation in Chapter 3.1 the range ambiguities are also calculated. The ambiguities are presented using the range ambiguity ratio, they can be found in Figure 3.2. To display the range ambiguity the ambiguities projections adjacent to the swath are plotted, they are seen via the two side lobes adjacent to the main beam. The closest ambiguous projection is shown in blue, the one after the swath in red. The antenna patterns that are used are sinc^2 shapes. They are roughly 40 dB attenuated compared to the signal level which is sufficient suppression.

In Figure 3.3 the geometry regarding the imaged area is presented. The line from the platform to the centre of the earth, which is perpendicular to the earth's surface, is called the nadir. The angle from the nadir to the imaged area is called the off nadir angle. The angle that the incoming beam makes with the earth's surface is called the grazing angle. The angle from the incident wave to a line perpendicular to the earth's surface at the swath is called the incidence angle. The orbit parameters related to Figure 3.3 are listed in Table 3.4.

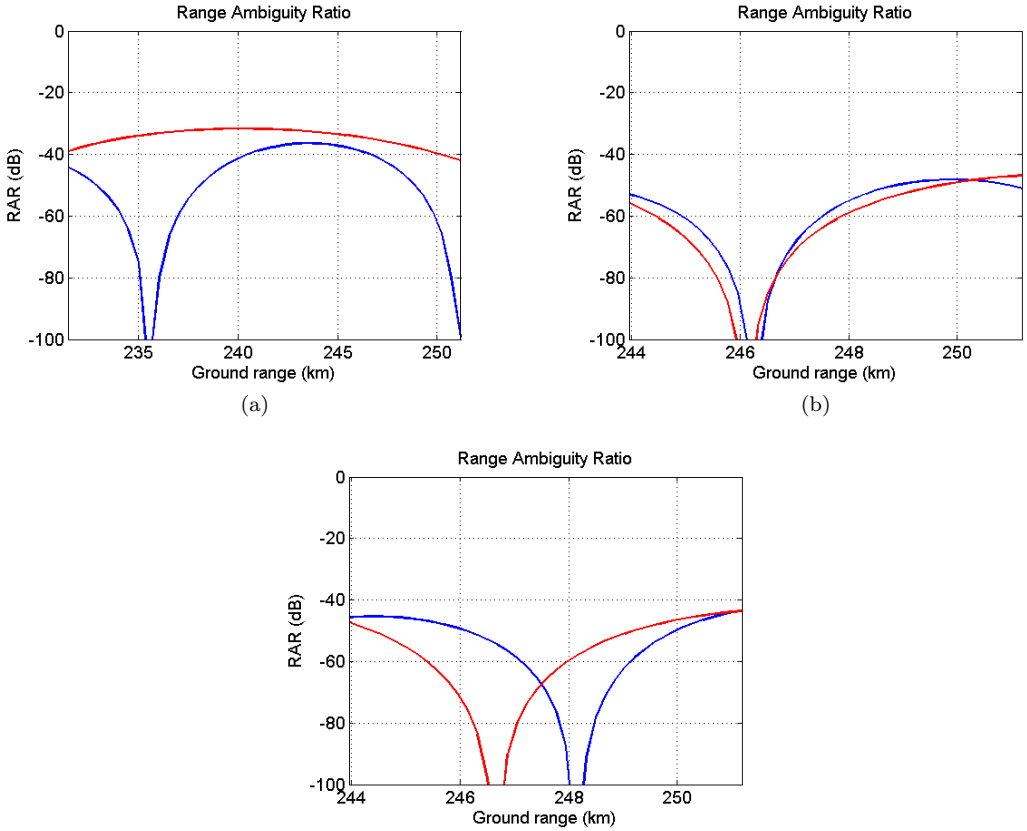

Figure 3.2: The range ambiguity ratios

Table 3.4: Orbit parameters of the satellite.

Variable	Value
Platform height	600 km
(Slant) Range	$639 - 655$ km

The swath of a satellite system is usually located at multiple times the ambiguous range of a radar system. Consequently the return from the nadir direction can appear in the final image of the swath. This happens if the distance to the nadir is shorter than the distance to the swath by (a multiple of) the ambiguous range. Since the dependence of the received power in the radar equation on the range is R^3, this causes the nadir return to be more powerful than the return from the swath. According to [12], if the nadir return appears in the swath it needs to have 44dB less power than the return from the swath to produce useful data. In that case the antenna pattern needs a zero in the direction of the nadir. If the ambiguous nadir return is placed before or after the return of the swath the contribution also can be filtered from the image. To ensure that the nadir return does not interfere with the desired return, the unambiguous range (D) needs to be known. It can be found from Equation 2.7. The nadir return can be moved away from the swath by changing the SRF.

Assume as example that the minimum SRF is required in the situation of Figure 3.3 with the parameters of Table 3.4. For a Sweep Repetition Frequency (SRF) in the order of $3 - 4$ kHz the unambiguous range is in the order of $37.5 - 50$ km. With a SRF of 3 kHz the unambiguous range is 50 km and the nadir return will be imaged at a slant range of 650 km. With an increase of

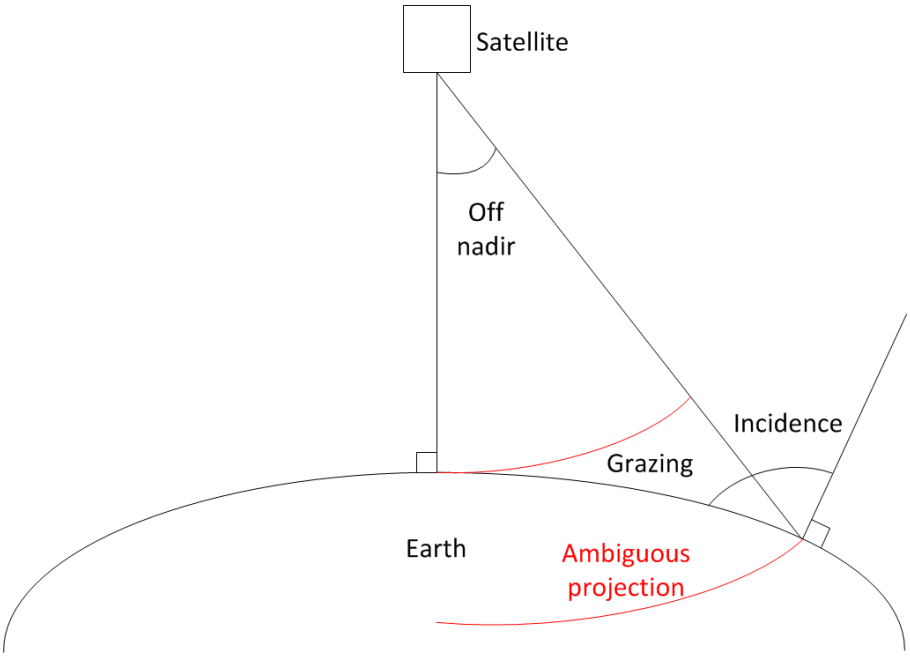

Figure 3.3: Geometry of the satellite system.

the SRF of 500 Hz, to 3.5 kHz, the unambiguous range is about 43 km and the nadir return is at 642 km. For 4 kHz the unambiguous range is 37.5 km and the nadir return is imaged at 675 km and has now shifted out of the swath. Due to the relatively high sweep repetition frequency the unambiguous ranges in the presented examples are relatively low. The unambiguous range is in these cases in the order of the difference in range between the swath and the nadir projection of the earth.

3.3 System Configurations

In Chapter 2 we discussed the FMCW technique. The advantages of an FMCW system are the simple electronics and the low peak power required. To create a FMCW SAR satellite there are multiple system configurations possible. For our system both mono-static and multi-static configurations are considered. The options that are considered are:

1. 1 antenna FMCW on 1 satellite
2. 1 antenna Gated FMCW on 1 satellite
3. 2 antennas FMCW on 1 satellite
4. 2 antennas FMCW divided over 2 satellites

The choice for the configuration also has impact on the hardware design. In Figure 3.4 the hardware schemes corresponding to the ”1 antenna FMCW on 1 satellite” option in (a), the ”2 antennas FMCW on 1 satellite” option in (b), and the ”2 antennas FMCW divided over 2 satellites” option in Figure (c) are presented. The hardware scheme for a gated FMCW option is slightly more complicated and would require some customisation to switch the signal generation on and off and still be able to down mix the received signal with the transmitted signal.

The first option is a satellite with a single antenna with connected Tx and Rx chains of which the block diagram is presented in Figure 3.4a. The signal is generated and amplified in the transmit chain and transferred via the circulator to the antenna. The received signal is transferred via the

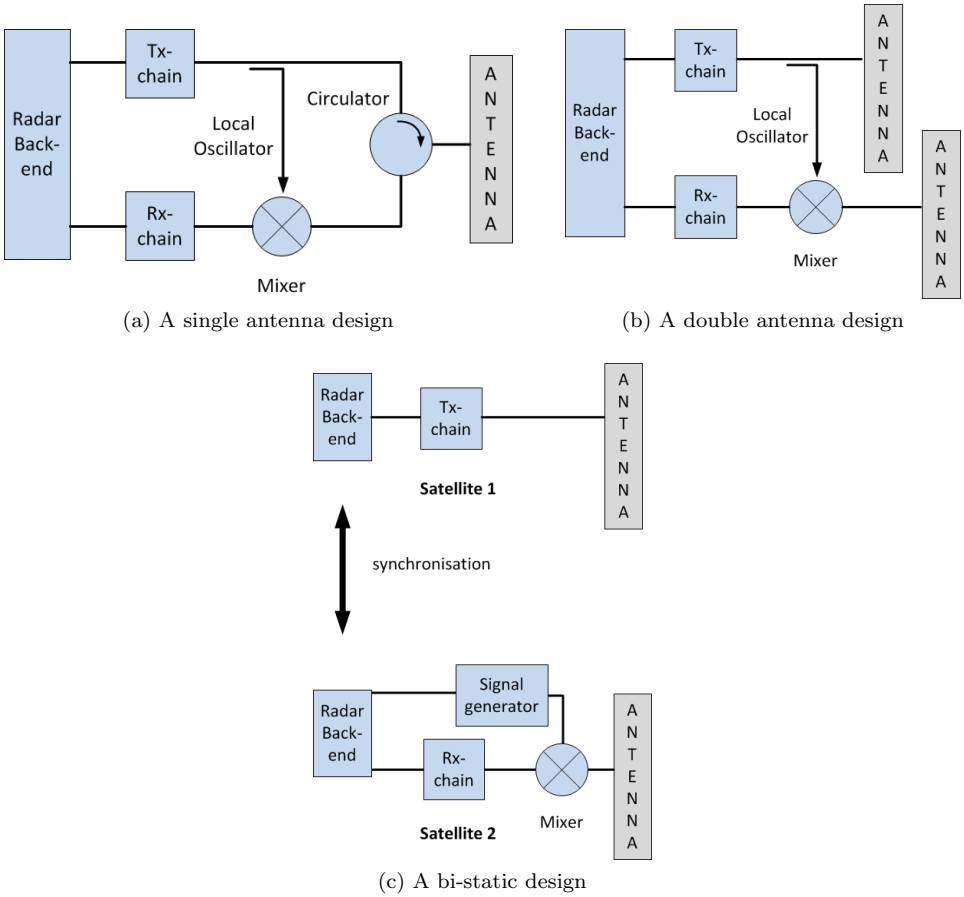

(a) A single antenna design

(b) A double antenna design

(c) A bi-static design

Figure 3.4: The system designs considered

same circulator to a mixer where it is mixed down with the transmitted frequency and inserted in the receive chain. In a conventional FMCW system with one antenna the circulator has to provide the isolation between the transmit and receive chain. The isolation a circulator can provide is in the order of 20dB. Since the transmit power in space applications is higher than in earth based applications, the isolation requirement is more stringent.

The received power that returns from the swath can be calculated using a modified version of the radar equation, Equation(3.1). In this modified equation the σ for a single target is replaced by the returns of the entire swath, $\sigma_0 \cdot R \cdot \theta_{az} \cdot R \cdot \theta_{elev}$. This modified equation is given by,

$$P_r = \frac{P_t G_t G_r \lambda^2 R^2 \theta_{az} \theta_{elev} \sigma_0}{(4\pi)^3 R^4 L_s} \,. \tag{3.6}$$

For a system as presented in Table 3.5 the total received power from the entire swath is in the order of -110 dBW for a sigma zero value of 0. This value is optimistic since it assumes that the power of all the separate range bins constructively adds up. A more conservative estimation of the power level is the power received from a single range bin like, used in pulsed radar systems. In that case the value that is substituted for the *sigma* value is $\sigma_0 \cdot R \cdot \theta_{az} \cdot \Delta R_g$. In that case if a ground range resolution of 4 m is used, the received power is -142 dBW for a σ_o value of 0. In our calculations the optimistic value -110 dBW is used. For scatterers with a low sigma zero value of -25, the received power level is about -135 dBW. A circulator that provides sufficient isolation to reduce the crosstalk from the transmit chain (+17.4 dBW) to the receive chain does not exist. Therefore a solution with single antenna and conventional FMCW is not feasible in

space applications.

An approach to overcome the problem of isolation in a mono-static solution with combined Tx/Rx modules can be found in [13]. This paper presents the gated FMCW technique. Gated FMCW uses a gating frequency, which is higher than the sweep repetition frequency to switch the transmitter on and off. If the beat frequency becomes higher than the gating frequency, the signal interferes with the IF of the system. The gating frequency f_g is given by

$$f_g = \frac{c}{2R_g}\,, \tag{3.7}$$

where R_g is the range associated with the gating window. The range needed in our application is 15 km. From (3.7) it follows that the maximum gating frequency is 10 kHz. For a functional gating scheme it is necessary that the swath is covered by the distance associated to the gating frequency. The maximum beat frequency (f_b) that is received is given by,

$$f_b = \frac{2R_{max}B}{cT_s}\,. \tag{3.8}$$

In which R_{max} represents the distance to the end of the swath, and T_s the sweep time. The minimum beat frequency can found from the distance closest to the platform. From the difference between the two values the bandwidth of the beat frequency can be obtained. For our system the bandwidth of the beat frequency is in the order of 20 MHz. This will result in a gating frequency that appears in the beat signal. Consequently the gating technique is not suitable for this system.

An interrupted FMCW scheme has also been considered. This scheme is analogue to the preceding approach, but the switching is carried out between sweeps instead of multiple times per sweep. The drawback of such a system is that the duty cycle of the transmitter is relatively low. This results in a lower average transmit power. According to (3.5) the transmit power per sweep needs to be increased to obtain the same averaged transmit power. Therefore, the interrupted scheme was not considered feasible.

If a single satellite with two antennas is used it is necessary to separate the transmit and receive chain, see Figure 3.4b for the corresponding block diagram. The design of such a satellite for our project is not possible within the satellite's size constraints. Moreover, the isolation is still a problem. However with a re-design is might be possible to fit two antennas and obtain sufficient isolation. The demands on the isolation between the transmit and received chain are mainly caused by phase noise limitations, the cross talk levels, and dynamic range limitations of the receiver.

For the option with one satellite and two antennas an example system is specified. The parameters for this system are shown in Table 3.5.

If we consider the same example as in the case with the circulator, the received power according to the radar equation is in the order of -110 dBW for a sigma zero value of 0. For scatterers with a low sigma zero value of -25, the received power level is about -135 dBW. With 100 dB isolation between the transmit and receive antenna the cross talk level is -83 dBW. A dynamic range for the receiver of 52 dB is required in this case. The number of bits of the A to D converter required to address the dynamic range is given by,

$$\text{ENOB} \approx \frac{\Delta D}{6.02}, \tag{3.9}$$

where ΔD is the dynamic range. For 52 dB the number of bits required for the A-to-D converter is 9. Although this is not very high, it will impact the downlink requirement seriously.

Another problem in FMCW radar is the phase noise that arises if there is not sufficient isolation between the transmitting antenna and the receiving antenna. It will cause the total noise level to be higher than just the thermal noise. The phase noise is usually added to the noise in the formula for the CNR, Equation 3.3. The phase noise originates from the oscillator and appears as difference between the phase of the oscillator and nearby received signal. In contrast to the

Table 3.5: Parameters of an example mono static satellite system

Variable	Value	Value in dB
Transmit power	55 W	17.4 dBW
Antenna gain T & R	-	46 dB
Wave length	0.03 m	-15.25 dB
Additional loss	-	3 dB
Sweep B	100MHz	-
SRF	5120 Hz	-
Distance to the swath	620 km	57.9 dB
Half power beam width in azimuth	0.0087 rad	-
Half power beam width in elevation	0.0106 rad	-
Illuminated area	35449368m^2	75.4 dB(m^2)
Noise figure	-	3 dB
$N_{ph,oc}$	-	$-130\,dBc/Hz$ at 20 MHz from the carrier
Separation of panels	2 m	-

thermal noise, increasing the transmitted power does not help. If the transmit power is increased the phase noise also increases. The phase noise is given by,

$$N_{ph} = P_t + N_{ph,oc} - I_{ant} + C_{ph}\,[dBm/Hz]\,, \tag{3.10}$$

with P_t the transmitted power in dBm, I_{ant} the isolation between the antennas, N_{ph_oc} the phase noise of the oscillator relative to the carrier in dBc/Hz and the correlation factor C_{ph} given by,

$$C_{ph} = 4(\sin(\pi f_b T_d))^2[]\,. \tag{3.11}$$

where f_b is the beat frequency in Hertz and T_d the time delay of the signal causing the phase noise in seconds.

Using the parameters of Table 3.5 and table 3.1 the phase noise at a beat frequency of 20 MHz is -111.8 dBW/Hz with an isolation of 0 considered. The thermal noise per Hertz bandwidth is given by,

$$N_{th} = kT_0F, \tag{3.12}$$

where k is the constant of Boltzmann, T_0 the system temperature and, F the noise factor. For a noise figure of 3 dB the thermal noise is -201 dBW/Hz. The difference between the thermal noise and phase noise is 89.2 dB for a beat frequency of 20 MHz. With a phase noise level of roughly 90 dB above the thermal noise level the system will not work. However if the isolation of 100 dB is present the phase noise will be below the thermal noise level. The phase noise is in this situation still present but affects the CNR not that much. In an FMCW system there is also AM noise present. However the amplitude noise is in general much lower than the phase noise. The level of AM noise is not available at the moment, and therefore not considered. In [6, Lecture 6] it is explained that the phase noise and AM noise both should be 12 dB below the thermal noise level to have a decrease in CNR of less than 0.5 dB. With 100 dB of isolation the phase noise is more than 12 dB below the thermal noise and therefore the phase noise will not be a major problem. However the phase noise will have a small impact on the performance of the presented system with two antennas on the same satellite.

The option with one satellite and two antennas is a promising option. However the required isolation of 100 dB is still hard to obtain and the size and weight of a satellite with two antennas might be an issue.

A bi-static solution is an alternative but, it requires two satellites to be launched, which is more expensive than launching a single satellite. However, it avoids the problem of isolation and it reduces the size, weight and power consumption of the single satellite.

The block diagram of the hardware of a bi-static solution is presented in Figure 3.4c. Since the transmit chain and the receive chain are divided over two satellites there is synchronisation

required between the transmitter ans the receiver. This synchronisation is quite difficult. Also there is the need for precise pointing of the two satellites. Both satellites should be pointing exactly to the same part of the swath to image the swath.

If the problems regarding the synchronisation and pointing can be resolved a bi-static solution is an easy way to avoid the problems of isolation.

3.4 Antenna Choice

For the final system the antenna needs to be selected. Besides impact on the radar performance the antenna choice also has impact on the weight, shape and internal power budget of the satellite. In the satellites design the following antenna options have been considered:

- Parabolic dish
- Reflect array
- Phased array
- Slotted waveguide centre fed, alternating offsets

In Chapter 3.1 the used elevation pattern for the antenna is a sinc^2 pattern. Using such a pattern is a good first approximation of the final antenna pattern. However for some antennas, like the parabolic dish, this approximation is not sufficiently accurate.

3.4.1 Parabolic Dish

The first option that was considered was the parabolic dish. A parabolic dish allows the spatial combining of power. This means that multiple feeds compose the total feed pattern. Consequently it is possible to divide the power demand over multiple amplification chains. Since the currently available low power HPA's are more power efficient compared to high power HPA's,the separate chains cause overall better efficiency. A dish with about 2 meters diameter is required to obtain the 3 m^2 antenna aperture required. However small antenna length in azimuth would result in a high PRF, which causes the ambiguous range to decrease. The size of a parabolic dish is a problem. A folded dish still takes a lot of space and may cause discontinuity in the surface of the unfolded parabola, resulting in pattern degradation. Another option is to use a metallic film to wrap around the ribs of the umbrella-like dish, as for example in tec-sar ([14]). Such a solution could also result in surface inaccuracy which has to be compensated. The estimated weight of such a structure is 21 kg based on the data of the tec-sar mission. Despite being smaller the folded umbrella like structure still turned out to be too big for the launcher. Getting the power to the feed is also an issue. If all the electronics are placed in the satellite, getting the signal to the feed in the focal point is a problem. If cables are used, the corresponding losses will have to be compensated. Another option is to use a waveguide for the power transfer from the satellite to the focal point of a 2.5 meter parabola. The length of such a waveguide exceeds the dimensions of the available space in the launcher. All the electronics related to signal generation can alternatively be placed in the feed. Then a thermal problem might occur since the generated heat cannot be radiated towards the cold space. The increase of electronics in the feed will result in a bigger feed. Consequently the feed blockage will have a bigger impact on the radiation pattern.

Table 3.6: Parameters used for the parabola

Variable	Value
Diameter	3 m
Distance to focal point	1.2 m
Frequency	9.5 GHz

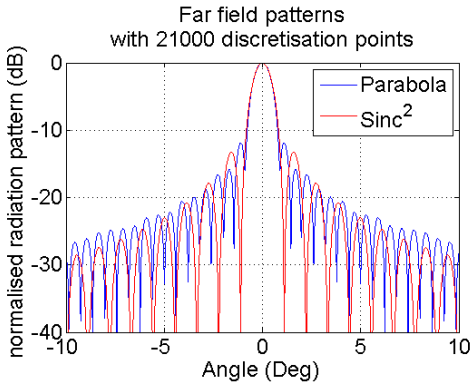

Figure 3.5: Far field radiation patterns of parabolic dish(blue) and sinc^2(red)

In Figure 3.5 the far field pattern for a parabola is shown and compared with a sinc^2 shape. The patterns for the parabola are generated using the codes of Balanis [15]. For the parabolic dish the main beam coincides with the sinc^2 pattern, the location for the side lobes shows a large deviation. The result for usage of the sinc^2 pattern for the range ambiguities will differ from the result with the parabola pattern.

The simulation of the parabolic dish using the codes of Balanis has a high computational burden. The code is inefficiently written, however for occasional use this is sufficient. The code calculates the entire beam pattern and stores it. If the normalized radiation intensity for a certain angle is required the nearest element of the results is filled in. If the parameters change often, the long times required for the generation of the patterns are not efficient and it might be useful to implement a dedicated function.

3.4.2 Reflect Array

An alternative to avoid problems regarding the size of the parabola in the launcher, is the usage of a reflect array. A reflect array is a passive or active antenna that consists of a planar array illuminated by a feed. The resonant patches reflect the beam of the feed thereby emulating a parabolic dish. This is achieved by tuning the separate patches with a microstrip transmission line. The microstrip line adjusts the phase to compensate for the different path length from the patch to the emulated location on the parabola. If the reflect array is active the patches have an active phase shifter and thus limited beam steering can be performed. In our case phase shifters are not desired since they would involve a lot of extra electronics. In our case a reflect array was considered consisting of passive patches on a Rogers ro5880 dielectric substrate. The material has a density of 2.2 g/cm^3. If this is applied to folded panels with a combined surface of 4.7 m $\times$ 0.9 m with a thickness of 0.6 mm, the weight of the panel is 5.6 kg. This weight is not including the patches and the feed. The disadvantage of the reflect array are the losses in the dielectric substrate, resulting in a lower total efficiency compared to the parabolic reflector, see [16].Reflect arrays are not used in space applications at the moment and they are therefore not marked as proven technology. The usage of proven technology in large space projects is often required to minimize the risk of failure. Due to the fact that the reflect array is not fully synthesised the far field patterns are not computed.

3.4.3 Active Array

An active array is also considered as an option. The main advantage of this solution is the ability of beam steering. The disadvantage is the amount of electronics needed to control all the separate patches. This amount can be reduced by introducing sub-arrays with corporate feed networks to divide the power over multiple elements. If micro strip lines are used this may lead to increased

feed line losses. The scanning capabilities of an active array are reduced if the phase shift of the patches can not be controlled separately, which is the case if sub arrays are used. The weight of such a solution is also an issue since the electronics will contribute to the mass of the antenna, the weight if the dielectric is roughly the same as in the case with a reflect array. This weight is larger than the weight of the reflect array due to the extra electronics involved for active arrays. Therefore the option with active array is not considered feasible.

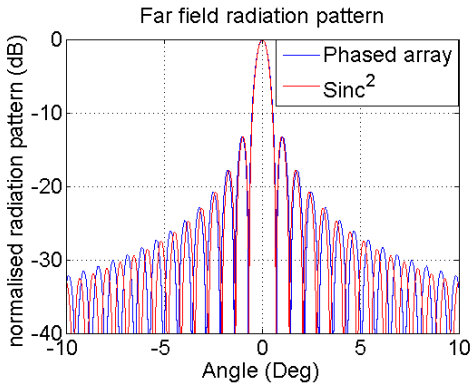

Figure 3.6: Far field radiation patterns of phased array(blue) and sinc^2(red)

Table 3.7: Parameters used for the phased array

Variable	Value
Width	1 m
Spacing	0.5λ
Frequency	9.5 GHz

In Figure 3.6 the far field patterns of the phased array and a sinc^2 shape are shown. For the phased array the far field pattern coincides with the sinc^2 pattern.

3.4.4 Slotted Waveguide Array

An other option is the slotted waveguide array. At first sight the slotted waveguide array seems relatively heavy compared to the other options mentioned. However according to [17] the waveguide wall can be as thin as 0.4 mm. The density of aluminium is 2.9 g/cm^3. Another option is carbon fibre re-enforced plastic (CFRP), the wall thickness for CFRP is 0.5 mm which has a density of 2.2 g/cm^3. The waveguides can be placed cascaded and share the middle wall. If the height of the waveguides is 1 cm the total weight will be 11.4 kg for aluminium and 9.1 kg for CFRP. An advantage compared to the active array is that a slotted waveguide has less feed line losses, since the power is transferred via the waveguide. A disadvantage of CFRP lies in the manufacturing process, the result is not as smooth as aluminium.

A slotted waveguide array consists of a waveguide with slots carved in one of the walls. The waveguide can be fed from the end or from the centre. If the frequency that is transmitted differs from the frequency that the waveguide is designed for, the transmitted pattern will be squinted. This is due to the fact that the location of the slot is determined and tuned for one particular wavelength. Centre feeding minimizes this problem since, at the end of the array the mismatch will be half the mismatch of a similar end fed wave guide. Since the maximum length of an array is determined by the tuning of the slots, centre feeding can reduce the amount of electronics needed.

Within TNO there is a code available to simulate the far field pattern of the slotted waveguide array. However this code does not take in to account the mutual coupling of the slots. For proper estimation of the system performance it is required to have precise far field patterns that can be

generated fast to be able to evaluate different designs rapidly. The code that is available within TNO is a good first approximation, however far field patterns that include the mutual coupling are desired for more reliable results. The derivation for the model of a slotted waveguide array and the corresponding far field patterns are presented in Chapters 4 and 5.

3.4.5 Simulation Software

To create precise antenna patterns in the code used to generate the pictures of Chapter 3.1 a antenna pattern code has been generated within the context of this thesis. The code generated is capable of calculating a sinc^2 pattern, the pattern of a parabolic dish and of a phased array with or without surface errors. The code can be extended with other patterns.

Since the computation of the pattern requires a lot of time and the computation can not be done for any random angle while the program is running, the patterns need to be precomputed. This is done by using functions that run in the beginning of the program and pass the data to the function. The initialisation can be done with a struct to pass the parameters for the different antennas to a sub function. The sub function checks if there are variables that have changed compared to an existing datafile. The parameters passed to the function via the struct are the parameters specific for the different antenna, like in the case of the parabola the distance from the feed to the dish. The global parameters are declared in the function that generates the antenna patterns. If a value of the pattern is required, an other function is called with the antenna type and an angle. The function then returns the value of the normalized gain pattern closest to the demanded value.

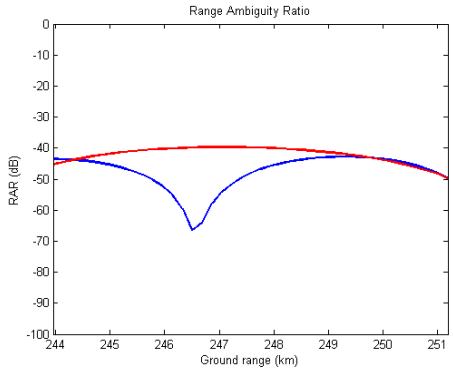

Figure 3.7: RAR for parabolic dish

In Figure 3.7 the range ambiguity ratio curves are shown with the utilisation of the specific antenna patterns. Like in Chapter 3.2 the range ambiguity is shown for the closest ambiguous projection in blue and the one after the swath in red. As can be seen in Chapter 3.4.1, the beam patterns do not always coincide for the side lobes. Also it can be observed that curves are not entirely fluent this is due to the number of far field discretisation points in the pattern. This can be observed around the zeros in the far field pattern. The number of discretisation points has been a choice based on computational time and usability of the result. The ambiguity levels are in this example also sufficiently low to have a feasible system.

3.4.6 Hardware

In the final system the technological readiness, the efficiency, off the shelf availability of electronic components play an important role in the selection process. Considering the efficiency of the different options, we observe that the efficiency of a reflect array antenna is relatively low compared to the parabolic dish antenna or the slotted waveguide antenna. The same is valid for active array

antennas. Therefore our preference is for a slotted waveguide array. The generating of the far field patterns of the slotted waveguide array is discussed in the next chapters.

Due to the choice for the slotted waveguide antenna, the form factor and the demands on the electronics can be worked out in further detail. In Figure 3.8 an illustration of an antenna tile is

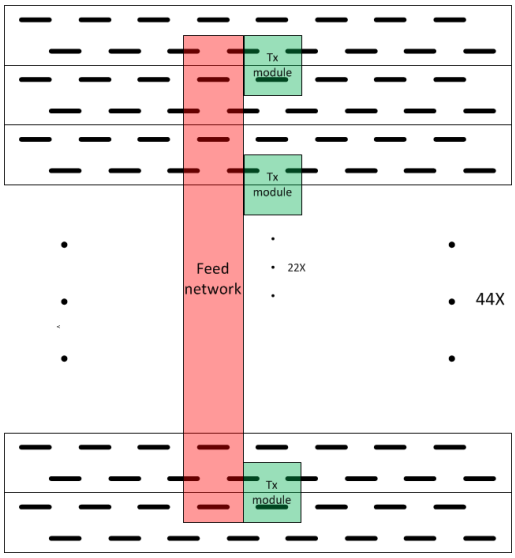

(a)

Figure 3.8: The feed network for the slotted waveguide arrays

shown. The amount and weight of the electronics involved in feeding all the waveguides separately is still a concern. To save on the weight of the electronics and utilize available high efficiency (High) Power amplifiers ((H)PA), the waveguides are going to be excited per two waveguides.

The electronics with reference to Figure 3.4b of the Tx chain for our system, consists of the following components:

- Pulse generator
- Phase shifter
- Medium power amplifier (MPa) and power amplifier (Pa)
- Power divider

In our system the phase shifter is present to enable beam steering or perform pattern reconstruction. As shown in Figure 3.9 the phase shifter is connected to two waveguides therefore the beam steering can cause lobes and only rough corrections to the pattern can be made. The medium power amplifier and the power amplifier provide a two stage amplification of the signal. Because of the separate transmit and receive chains in our system the circulator is not necessary. The Rx chain in Figure 3.4b typically consists of several low-noise amplifiers (LNAs) and a phase shifter per antenna element.

In the following table, Table 3.8 the power budget for one transmit chain is presented. The total power required for one transmit chain like in Table 3.8 is 1420 mW. Assuming 22 amplification chains the total power required for the 5 tiles becomes $(22 \cdot 1.420 + 0.025) \cdot 5 = 156.33$ W this includes one micro controller per tile to control the phase shifters. The system losses are 16 dB, with the losses of the divider network to get the power to the separate chains included. The transmitted power for the entire antenna is according to the output signal level about 62 W. For the receive chain similar analysis can be performed. The level of the signal at the terminals of a single waveguide is estimated at -133 dBW (-103 dBm), based on a received power of -110 dBW

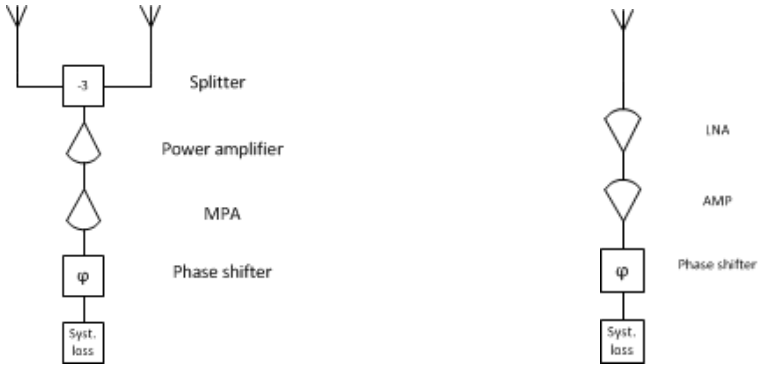

Figure 3.9: Transmit chain(a) and receive chain(b) schematic

Table 3.8: Overview of transmit chain

	Linear value	Value in dB	Signal level after stage	Supply voltage	Power consumed
Input RF	10m W	10 dBm	10 dBm	-	-
System losses	0.025	−16 dB	−6 dBm	-	-
Phase shifter	0.2	−7 dB	−13 dBm	10 V	120 mW
PA1	40	16 dB	3 dBm	10 V	40 mW
PA2	316	25 dB	28 dBm	12 V	1260 mW
Divider loss	0.9	0.5 dB	24.5 dBm	-	-

divided over 220 waveguides. The output power of −88 dBm before the combiner. In a practical system the gain of a amplification chain should be roughly 30 dB to minimize the effects on the noise figure, in this example only 15 dB of amplification is obtained. The 30 dB of amplification can be obtained by increasing the amplification of the LNA. Also there should be noted that the estimation of the system losses is rather high and also include the losses in the combiner network.

The total power required for a receive chain like in Table 3.9 is 200 mW. The total for the 5 tiles is over 44 W, this includes one micro controller per tile to control the phase shifters. This is a lot of power for the receive chain considering the fact it also needs to be sampled, processed and, sent to the earth, which all consumed power as well.

3.5 Downlink

A real-time data downlink is one of the requirements on the system. The sample rate of our system is 50 MHz. The minimum number of bits for the A to D converter is 9, this is explaned in in Section 3.3. This can be compressed using Block Adaptive Quantization(BAQ). The compression operates on blocks of data. First the general characteristics of the block are determined. Then a smaller number of bits is used to quantize the data in the block. More about BAQ can be found in [18]. After compression using BAQ the remaining data rate of our system will be 3 bits per sample.

The data rate that needs to be downlinked including overhead is about 200 Mb/s. A commercially available system capable of performing this task is developed by Surrey space systems [19]. The system has an agile horn antenna with a gain of 15 dB, consumes 60 W, operates at X-band, and weighs 6 kg. Such a system would not be suitable for this project since it would be rather heavy and consumes relatively much power. An alternative would be a 2 dimensional patch array with 16 patches. This alternative was selected for the low profile and the low weight of such a solution. The number of patches follows from the demand for a half power beam width of 40°. It

Table 3.9: Overview of receive chain

	Linear value	Value in dB	Signal level after stage	Supply voltage	Power consumed
Received RF	− mW	−103 dBm	0 dBm	-	-
Lna	125	21dB	−82 dBm	4 V	40 mW
Pa	100	20 dB	−62 dBm	4 V	40 mW
Phase shifter	0.2	−7 dB	−69 dBm	10 V	120 mW
System losses	80	−19 dB	−88 dBm	-	-

can be calculated using [15, Eq.6.14] that the half power beam width at broadside in azimuth and elevation is about 45° for 4 patches in both directions.

In order to find a suitable modulation scheme for the downlink a value for the $\frac{E_b}{N_0}$ need to be found. The $\frac{E_b}{N_0}$ value is called the bit energy. It is a measure for the energy to noise ratio of a single bit. The $\frac{E_b}{N_0}$ can be used to determine the expected bit error rate for a data link with a given modulation. The $\frac{E_b}{N_0}$ for a data link can be calculated using equation (3.13)

$$\frac{E_b}{N_0} = \frac{P_t G_t G_r G_{fs}}{kTR_{data}}, \tag{3.13}$$

where G_t is the transmit antenna gain, G_R the receive antenna gain, R_{data} the data rate on the link and G_{fs} the free space gain. The free space gain is given by $\left(\frac{\lambda}{4\pi R}\right)^2$, with R the range.

Table 3.10: System parameters for the downlink.

Variable	Value
Transmit power	6 W
Transmit antenna gain	15 dB
Receive antenna gain	50 dB
T_{sys}	45 K
Data rate	200 Mbit/s

Inserting the parameters of Table(3.10) in Equation (3.13) and using a platform height of 570 km, the resulting $\frac{E_b}{N_0}$ is 34.7 dB. There has to be noted that Equation (3.13) only takes the free-space loss into account. According to Chapter 6.1 of [20] for frequencies above 3 GHz the contribution of the attenuation in the troposphere needs to be taken in to account, the contribution of the ionosphere can be neglected. The added attenuation for X-band is in the order of 0.005 dB/km. For the 10 km of troposphere the total added attenuation is in the order of 0.05 dB. In X-band there is also rain attenuation ranging from 0.05 dB/km for 2.5 mm/h to 10 dB/km for 150 mm/h. The rain attenuation can prevent successful downlinking of the data in heavy rain. However the rain is often close to the earth and if a ground station is not capable of receiving the data the satellite can use the beam steering to transmit the date to another ground station where it is not raining.

In satellite downlink systems the commonly used modulation schemes are based on Phase Shift Keying (PSK). In [21] a table is provided that links the $\frac{E_b}{N_0}$ to the bit error rate. The highest commonly used modulation technique is 16-psk, which requires an $\frac{E_b}{N_0}$ of 21.1 dB for an error probability of 10^{-10}. Since the $\frac{E_b}{N_0}$ is 34.7 dB in our system the transmit power of 6 W is sufficient. In such a system there is over 13 dB of margin in the power budget. For example that margin can be used to lower the power of the downlink system or can be used for robustness against rain attenuation.

To obtain the required transmit power of 6 W an amplification chain like in Chapter 3.4.6 can be used. If each of the 16 patches is connected to its own amplification chain lossy divider networks can be avoided. The system losses are estimated at 14.5 dB, including the losses in

the divider network. The parameters for one chain are presented in Table 3.11. The total power required for the amplification chains is 22.7 W, with a transmitted power of 14.3 W. The 14 W of transmit power should be sufficient for our system. The required input power for the system is considerably lower than the required power for the commercially available system. Therefore the presented alternative is a feasible option for a small satellite.

Table 3.11: Overview of downlink chain

	Linear value	Value in dB	Signal level after stage	Supply voltage	Power consumed
Input RF	10m W	10 dBm	10 dBm	-	-
System losses	0.025	−14.5 dB	−4.5 dBm	-	-
Phase shifter	0.2	−7 dB	−11.5 dBm	10 V	120 mW
PA1	40	16 dB	4.5 dBm	10 V	40 mW
PA2	316	25 dB	29.5 dBm	12 V	1260 mW

Chapter 4

Analysis of Slotted Waveguide Antennas

In this chapter, we develop a model for slotted waveguide arrays. With this model it is possible to obtain slot voltages of a slotted waveguide rapidly. This model will be used in the next chapter to generate a code for rapid simulation of a slotted waveguide array In order to obtain accurate far field patterns rapidly. Since there exists a vast amount of literature on the modeling and analysis of such arrays, we shortly discuss the references relevant for our work in Section 4.1. Next, we detail the geometry of a single waveguide with longitudinal slots in Section 4.2. Subsequently, in Section 4.3, we derive a system of equations for calculating the slot voltages. This derivation is based on electromagnetic field considerations and transmission-line concepts, and relies on earlier work by Elliott and others on two design equations for slotted waveguide arrays. In the work of Elliott the self coupling of a slot is a measured value and the mutual coupling was calculated. Finally, in Section 4.3.4 we pay particular attention to the calculation of the self admittance of a longitudinal slot, which are used in the self-coupling terms of the earlier derived system of equations.

4.1 Literature

The analysis of slotted waveguides started in 1957 with the papers of Oliner [22] and [23]. In these papers an approximation of the self admittance of longitudinal, displaced, and rotated slots is described. In particular for the approximation of the self susceptance, Oliner employs asymptotic arguments. Yee continued this work and improved the expressions of Oliner in [24] by employing the Green's function or kernel of a waveguide. Yee's series expansion of the susceptance has a few errors, which were resolved in an analysis carried out in parallel to our project [25]. The mutual coupling of slots on a waveguide was first considered by Elliott in [26] and [27]. The focus of these papers is on the design of the waveguide arrays resulting in two design rules, and the self coupling was at that time still obtained by measurements. Elliott's theory can particularly be used for determining the slot offsets given certain pattern specifications. Hammadallah combined Elliott's design rules to analyze slotted-waveguide arrays and in particular to compute rapidly their radiation patterns. To this end he developed both a recursive and a direct method for calculating the mode voltages. In later papers, for instance [28], Elliott and others discussed the software analysis of the slotted waveguide arrays using the method of moments.

Currently there are commercial solvers on the market that are capable of simulating a slotted waveguide array such as HFSS. In general however these solvers are not suitable for rapid prototyping due to the long computational times. A dedicated software tool for slot array analysis is SWAN. Due to unavailability this tool has not been investigated further. Instead we developed our own rapid-prototyping code based on the theory in the following sections. Finally, for an extensive literature review of slotted waveguide arrays we refer the reader to the paper of Rengarajan and others [29].

4.2 Geometry

To obtain an appropriate electromagnetic model for a slotted waveguide array we first define the geometry of such a waveguide array. Figure 4.1 shows the geometry of a waveguide with a single slot oriented parallel to the longitudinal direction of the waveguide. In our application we deal with an array of slots that are all parallel to this direction. For each slot we denote its length, width, and centre by $2\ell_q$, $2w_q$, and $\boldsymbol{c}_q$, where $q = 1, \ldots, Q$ with Q the number of slots of the array. The width and height of the waveguide are denoted by a and b. We introduce a Cartesian coordinate system whose origin is placed in the lower right corner of the waveguide intersection. Classically, the x, y, and z axes are directed along the width, height, length of the waveguide.

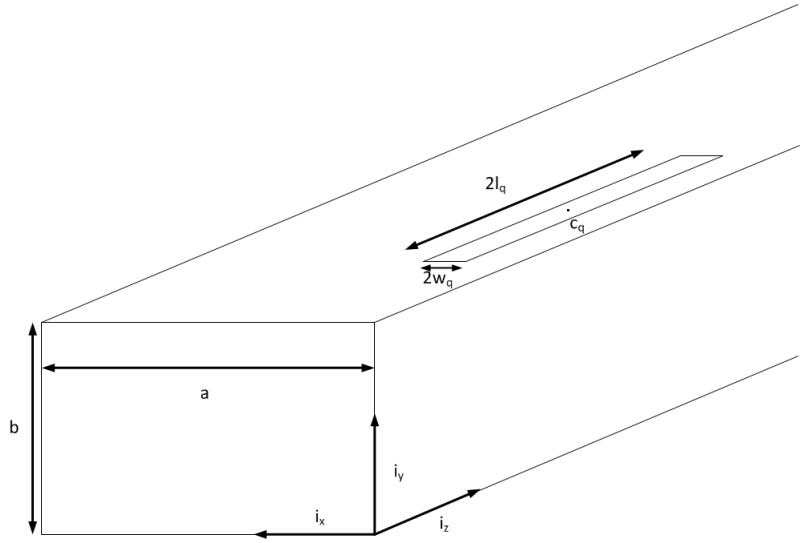

Figure 4.1: Geometry of a waveguide with a single slot oriented parallel to the longitudinal direction of the waveguide.

Figure 4.2 shows a top view of the slotted waveguide, which has two different slots labelled p and q and their surfaces are denoted by S_p and S_q. For our analysis in the next section, two waveguide intersections $S_{1,q}$ and $S_{2,1}$ are indicated at the two ends of slot q with axial coordinates $z = z_{1,q}$ and $z = z_{2,q}$. The surface of the slot is parametrised by

$$\boldsymbol{x}_{S_q}(\zeta, \xi) = \boldsymbol{c}_q + \xi \boldsymbol{i}_x + \zeta \boldsymbol{i}_z \,, \qquad -w_q \le \xi \le w_q, \, -\ell_q \le \xi \le \ell_q \,. \tag{4.1}$$

4.3 Electromagnetic Model

In the waveguide, time-harmonic wave propagation occurs along its longitudinal or z-direction with radian frequency ω. The corresponding electromagnetic field is governed by Maxwell's equations in the frequency domain, which are detailed in Appendix A. This field can be classically decomposed into transverse electromagnetic modes denoted by TE_{mn} and TM_{mn}. We assume that the waveguide is designed such that only the TE_{10} mode propagates. The complex field $(\boldsymbol{E}_{10}, \boldsymbol{H}_{10})$ of this mode is given by

$$\begin{aligned} H_{10,z}(\boldsymbol{x}) &= j \cos \frac{\pi x}{a} \, e^{\mp j \beta_{10} z} \,, \\ H_{10,x}(\boldsymbol{x}) &= \mp \frac{\beta_{10} a}{\pi} \sin \frac{\pi x}{a} \, e^{\mp j \beta_{10} z} \,, \\ E_{10,y}(\boldsymbol{x}) &= \frac{\omega \mu_0 a}{\pi} \sin \frac{\pi x}{a} \, e^{\mp j \beta_{10} z} \,, \end{aligned} \tag{4.2}$$

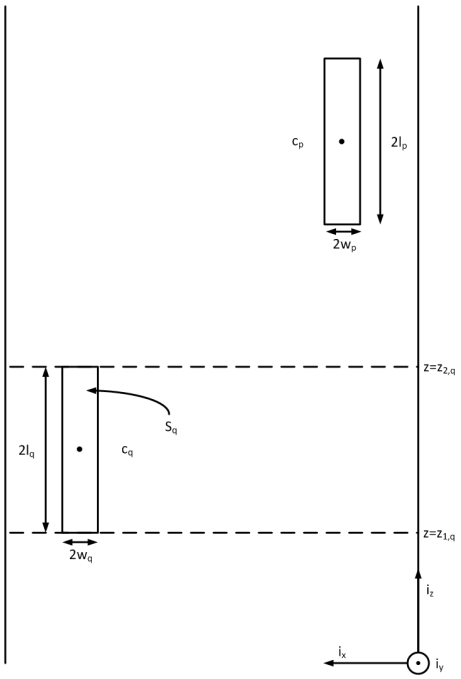

Figure 4.2: Top view of a waveguide with two slots.

where β_{10} is the wavenumber corresponding to the mode, i.e., $\beta_{10} = \sqrt{k^2 - (\pi/a)^2}$ with $k = \omega\sqrt{\mu_0\varepsilon}$, and where the upper and lower signs in $\mp$ are selected for propagation in the positive and negative directions, respectively. The other field components are zero. The propagating mode in the waveguide radiates through the slots. To describe the radiation mechanism, Elliott derived a circuit formulation composed of two design equations from field considerations [27, 26]. Hamadallah summarized and combined the two design equations to obtain a matrix equation from which the voltages generated at the slots can be resolved [30]. We discuss here first the derivations of the two design equations and then derive the matrix equation.

4.3.1 The First Design Equation

Elliott's derivation of the first design equation starts with the calculation of the backward and forward scattering coefficients of the TE_{10} mode at a slot. Focusing on the qth slot, the backward scattering coefficient [26, Eq. (4)] is given by

$$B_{10,q} = \frac{\int_{S_q} (\boldsymbol{E}^{\mathrm{slot}} \times \boldsymbol{H}_{10}) \cdot \boldsymbol{i}_y dS}{2 \int_{S_{1,q}} (\boldsymbol{E}_{10,\mathrm{t}} \times \boldsymbol{H}_{10,\mathrm{t}}) \cdot \boldsymbol{i}_z \, dS} \,, \tag{4.3}$$

Here ($\boldsymbol{E}^{\mathrm{slot}}$,$\boldsymbol{H}^{\mathrm{slot}}$) is the field that originates from the scattering of the incident mode at the slot and ($\boldsymbol{E}_{10}$,$\boldsymbol{H}_{10}$) is the field of the TE_{10} mode in (4.2), but propagating in the negative z-direction. The subscripts $_{\mathrm{t}}$ indicates the transverse field components, which are in our case $H_{10,x}$ and $E_{10,y}$ without the exponential. Analogously, the forward scattering coefficient is given by

$$C_{10,q} = \frac{\int_{S_q} (\boldsymbol{E}_{\mathrm{slot}} \times \boldsymbol{H}_{10}) \cdot \boldsymbol{i}_y \, dS}{2 \int_{S_{2,q}} (\boldsymbol{E}_{10,\mathrm{t}} \times \boldsymbol{H}_{10,\mathrm{t}}) \cdot \boldsymbol{i}_z \, dS} \,, \tag{4.4}$$

where the TE_{10} mode propagates in positive z-direction. The transverse components of the field representation (4.2) is substituted in the denominator of (4.3) and the integral is analytically

calculated,

$$\int\limits_{S_1,q} (\boldsymbol{E}_{10,\mathrm{t}} \times \boldsymbol{H}_{10,\mathrm{t}}) \cdot \boldsymbol{i}_z \, dS = \frac{\omega\mu_0\beta_{10}a^2}{\pi^2} \int\limits_0^b dy \int\limits_0^a \sin^2 \frac{\pi x}{a} \, dx = \frac{\omega\mu_0\beta_{10}a^3 b}{2\pi^2} \tag{4.5}$$

In the slot the electric field is mainly directed from one of its long sides to the other one. Since $\ell_q \gg w_q$, we may assume that the electric field is directed along the $x-$axis and is thus perpendicular to the long sides of the slot. Moreover we may assume that the field is uniform in $z-$direction and thus only depends on x. Consequently,

$$\boldsymbol{E}_q^{\mathrm{slot}} = E_{q,x}^{\mathrm{slot}}(\zeta)\boldsymbol{i}_x \, . \tag{4.6}$$

Substituting this expression in the numerator of (4.3) together with the magnetic field of the TE_{10} mode we obtain

$$B_{10,q} = -\frac{j\pi^2}{\omega\mu_0\beta_{10}a^3 b} \int\limits_{-w_q}^{w_q} \cos \frac{\pi(c_{q,x}+\xi)}{a} \, d\xi \int\limits_{-\ell_q}^{\ell_q} E_{q,x}^{\mathrm{slot}}(\zeta) e^{-j\beta_{10}\zeta} \, d\zeta \tag{4.7}$$

Note that we employ $2w_q$ as width of the slot instead of w as in [27, 26]. Focusing on the integral over ξ, we derive

$$\begin{aligned} \int\limits_{-w_q}^{w_q} \cos \frac{\pi(c_{q,x}+\xi)}{a} \, d\xi = \cos \frac{\pi c_{q,x}}{a} \int\limits_{-w_q}^{w_q} \cos \frac{\pi\xi}{a} \, d\xi = \frac{2a}{\pi} \cos \frac{\pi c_{q,x}}{a} \sin \frac{\pi w_q}{a} \; = \\ = -\frac{2a}{\pi} \sin \frac{\pi(c_{q,x}-a/2)}{a} \sin \frac{\pi w_q}{a} \approx -2w_q \sin \frac{\pi(c_{q,x}-a/2)}{a} \, , \end{aligned} \tag{4.8}$$

where we employ that $\pi w \ll a$, i.e., the slot width is much smaller than the waveguide width. The quantity $c_{q,x} - a/2$ in this expression is the offset of the slot with respect to the centreline of the waveguide, which is denoted by x in [26, Eq. (6)]. Subsisting the result for the integral over ξ into (4.7) and introducing the field distribution

$$E_{q,x}^{\mathrm{slot}} = \frac{V_q^{\mathrm{slot}}}{2w_q} \cos \frac{\pi\zeta}{2\ell_q} \, , \tag{4.9}$$

we obtain

$$B_{10,q} = \frac{j\pi^2 V_q^{\mathrm{slot}}}{\omega\mu_0\beta_{10}a^3 b} \sin \frac{\pi(c_{q,x}-a/2)}{a} \int\limits_{-\ell_q}^{\ell_q} \cos\left(\frac{\pi\zeta}{\ell_q}\right) e^{-j\beta_{10}\zeta} \, d\zeta \, . \tag{4.10}$$

For the integral we derive

$$\begin{aligned} \int\limits_{-\ell_q}^{\ell_q} \cos\left(\frac{\pi\zeta}{2\ell}\right) e^{-j\beta\zeta} \, d\zeta = \int\limits_{-\ell_q}^{\ell_q} \cos\left(\frac{\pi\zeta}{2\ell}\right) \cos(\beta_{10}\zeta) \, d\zeta \; = \\ = \frac{1}{2} \int\limits_{-\ell_q}^{\ell_q} \left[\cos\left(\left(\frac{\pi}{2\ell_q} + \beta_{10}\right)\zeta\right) + \cos\left(\left(\frac{\pi}{2\ell_q} - \beta_{10}\right)\zeta\right) \right] d\zeta = \frac{2\pi/\ell_q}{(\pi/2\ell_q)^2 - \beta_{10}^2} \cos(\beta_{10}\ell_q) \, . \end{aligned} \tag{4.11}$$

Substituting this result in (4.10) we obtain

$$B_{10,q} = \frac{j\pi^2 V_q^{\mathrm{slot}}}{\omega\mu_0\beta_{10}a^3 b} \frac{2\pi/\ell_q}{(\pi/2\ell_q)^2 - \beta_{10}^2} \cos(\beta_{10}\ell_q) \sin \frac{\pi(c_{q,x}-a/2)}{a} \, . \tag{4.12}$$

This expression can also be written as

$$B_{10,q} = -K f_q V_q^{\text{slot}} \,, \tag{4.13}$$

where

$$K = \frac{2(\pi/a)^2}{j\omega\mu_0\beta_{10}kab} \,, \tag{4.14}$$

and

$$f_q = \frac{\pi/2k\ell_q}{(\pi/2k\ell_q)^2 - (\beta_{10}/k)^2} \cos(\beta_{10}\ell_q) \sin\frac{\pi(c_{q,x} - a/2)}{a} \,. \tag{4.15}$$

This expression is the same as [26, Eq. (7)]. Since we have assumed the field in the slot symmetrical, see (4.9), the forward and back scattered fields are the same and thus $B_{10,q} = C_{10,q}$. As Elliott observes this symmetrical scattering is analogous to the scattering from a shunt element on a transmission line. Figure 4.3 shows the corresponding equivalent circuit of such an element. In this particular case, the load admittance Y_L is the admittance of the slot, the transmission-line admittance Y_0 is the admittance of the TE_{10} mode in the waveguide and the input admittance Y_{in} is the input admittance in the waveguide at a specific distance from the slot. Since the TE_{10} mode is in general propagating, we have $Y_0 = G_0$ with G_0 the conductance of the TE_{10} mode. Modelling the slot with label q in terms of its active admittance Y_q^{act} on an equivalent transmission line with conductance G_0, we obtain the forward and backward scattering coefficients

$$B = C = -\frac{1}{2}\frac{Y_q^{\text{act}}}{G_0} V_q \,, \tag{4.16}$$

where V_q is the mode voltage at the position of the shunt element represented by the active admittance Y_q^{act} of the slot. This relation is derived in [27, Sec. 8.14] with the aid of transmission-line results of [27, Sec. 3.6]. Elliott links the expressions (4.13) and (4.16) by requiring that $B_{10,q}$ and B have the same phase at any cross section of the waveguide and that the backscattered power levels are equal, which leads to his first design equation

$$\frac{Y_q^{\text{act}}}{G_0} = K_1 f_q \frac{V_q^{\text{slot}}}{V_q} \tag{4.17}$$

with

$$K_1 = -\frac{j\lambda}{a}\sqrt{\frac{2k/k_0}{\eta_0 G_0 \beta_{10} kab}} \,. \tag{4.18}$$

Neither in [26] nor in his book [27] Elliott presents a derivation of this last step. For details on the derivation we refer to [25].

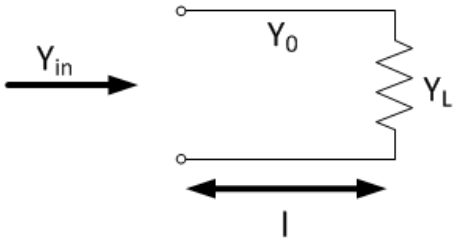

Figure 4.3: Equivalent circuit with input admittance Y_{in}, load admittance Y_L, and transmission-line admittance Y_0.

4.3.2 The Second Design Equation

In this section we summarize stepwise the derivation of the second design equation as described in [26].

1. One slot is considered open, say the slot with label q. The other slots are covered with conducting tape.

2. First the case of a propagating TE_{10} mode with amplitude $A_{10,q}$ and incident from $z = -\infty$ is considered.

3. A relation between the equivalent scheme and coefficients $A_{10,q}$ and $B_{10,q}$ is established, where $B_{10,q}$ is the coefficient of the back-scattered TE_{10} mode at the slot with label q [26, Eq. (13), (14)]; the waveguide is terminated in a matched load beyond the slot.

4. As in the previous section it is assumed that the scattering at the slot is symmetrical by which the forward-scattered coefficient $C_{10,q}$ is obtained as $C_{10,q} = B_{10,q}$. Moreover, for the coefficient of the TE_{10} mode incident from $z = +\infty$, the same relation is valid as the one between $B_{10,q}$ and $A_{10,q}$.

5. The slot voltage is decomposed in 3 components, one due to $A_{10,q}$, one due to $D_{10,q}$, and the last one due to the coupling with the other slots [26, Eq. (15)]. The first two voltages are derived straightforwardly [26, Eq. (16), (17)]. The third one is derived by employing the reciprocity theorem [26, Eq. (18)], which requires the specification of two situations.. We describe the corresponding steps:

   5a. In the first situation all slots except one are covered with conducting tape. The incident mode propagates from $z = -\infty$ with modal coefficient $A^{(1)}_{10,q}$. $B^{(1)}_{10}$. Note that Elliot denotes these coefficients by A^a and B^a, but in his notation the superscript a denotes also the active situation in e.g. [26, Eqs. (9), (10)]. Equivalent currents are defined at $z = z_1$ in the waveguide (with cross section S_1) such that, according to the extinction theorem, only a non-zero field is present beyond the sources. Here $z_1 < c_z - \ell$. We call that c_z is the z-coordinate of the center of the slot and ℓ is its half length.

   5b. In the second situation magnetic sources are placed at the locations of the other slots. These sources excite the slot under consideration by a wave with amplitude $B^{(2)}_{10,q}$.

   5c. The reciprocity integral is decomposed into an integral over the equivalent currents in the first situation and the fields in the second situation, and a sum of integrals over the magnetic currents in the slots in the second situation and the magnetic fields at the slots in the first situation [26, Eq. (22)].

   5d. The first integral is analytically calculated by substition of the field expressions of the TE_{10} mode with coefficient $B^{(2)}_{10,q}$ and the field expressions of the equivalent currents. The reciprocity theorem then results in an expression for $B^{(2)}_{10,q}$ in terms of the sum mentioned in the previous item.

   5e. To calculate the integrals in that sum, expressions for the magnetic fields at the slots in the first situation and for the magnetic currents at the slots in the second situation are required. The magnetic fields are calculated from the magnetic vector potential [26, Eqs. (26), (27)] with prescribed magnetic currents [26, Eqs. (25)]. These currents are chosen as cosine functions with coefficients the total slot voltages in the first situation. The magnetic currents in the second situation are similarly defined as cosine functions with coefficients the total slot voltages in the second situation.

   5f. Fields and currents are subsituted in the expression for $B^{(2)}_{10,q}$. Consequently, $B^{(2)}_{10,q}$ is expressed as a sum over double integrals with respect to the lengths of the slots. The integrand consists of the two currents (cosine functions) and the fundamental solution of the Helmholtz equation in free space $\exp(-jkR/R)$. Physically the integrals represent

the coupling between two slots with labels q and p. The result is denoted by the coupling coefficient G_{pq}.

5g. The coefficient $B^{(2)}_{10,q}$ is linked to the third voltage (see item 5) by the relation (4.13) derived for the first design equation.

6. Having obtained expressions for the three voltages, the active admittance of the slot Y^{act}_q is expressed in terms of the modal coefficients $A_{10,q}$, $B_{10,q}$, $C_{10,q}$, and $D_{10,q}$, whose expressions in terms of the voltages are employed to arrive at the second design equation.

The steps 5e – 5g and 6 are further detailed in [25], where also another expression for G_{pq} is derived than the expression obtained Elliott [26, Eq. (30)]. The final result for the second design equation reads

$$\frac{Y^{\mathrm{act}}_q}{G_0} = \frac{2f_q^2}{\dfrac{2f_q^2}{\dfrac{Y^{\mathrm{self}}_q}{G_0}} + j(\beta_{10}/k)(k_0 b)(a/\lambda)^3 \displaystyle\sum_{p=1,p\neq q}^{Q} \frac{V^{\mathrm{slot}}_p}{V^{\mathrm{slot}}_q} G_{pq}} \,. \tag{4.19}$$

Here Y^{self}_q is the self admittance of the slot in isolation. This admittance can be approximated by the theory developed by Oliner [22, 23] and Yee [24]. A summary of the results in terms of our notation is described in [26].

4.3.3 Derivation and Solution of a Matrix System for the Slot Voltages

In [30], the two design equations derived by Elliott are combined to a single matrix equation. This is accomplished as follows. The second design equation is written as

$$\frac{1}{Y^{\mathrm{act}}_q/G_0} = \frac{1}{Y^{\mathrm{self}}_q/G_0} + \frac{1}{K_2 f_q^2} \sum_{p=1,p\neq q}^{Q} \frac{V^{\mathrm{slot}}_p}{V^{\mathrm{slot}}_q} G_{pq} \,. \tag{4.20}$$

We note that in [30, Eqs. (1), (2)] the admittances are normalized to G_0. The constant K_2 can be determined from Elliott's version (4.19) of the second design equation by rewriting it as

$$\frac{G_0}{Y^{\mathrm{act}}_q} = \frac{G_0}{Y^{\mathrm{self}}_q} + \frac{j(\beta_{10}/k)(k_0 b)(a/\lambda)^3}{2f_q^2} \sum_{p=1,p\neq q}^{Q} \frac{V^{\mathrm{slot}}_p}{V^{\mathrm{slot}}_q} G_{pq} \,. \tag{4.21}$$

This form is the same as (4.20) if we identify K_2 as

$$K_2 = -\frac{2j}{(\beta_{10}/k)(k_0 b)(a/\lambda)^3} \tag{4.22}$$

The second design equation in the form (4.20) can be rewritten by substitution of the expression for the normalised active admittance Y^a_q/G_0 given by the first design equation (4.17). Multiplying subsequently the equation by $K_2 f_q^2 V^{\mathrm{slot}}_q$ we obtain

$$\frac{K_2}{K_1} f_q V_q = \frac{K_2 f_q^2}{Y^{\mathrm{self}}_q/G_0} V^{\mathrm{slot}}_q + \sum_{p=1,p\neq q}^{Q} V^{\mathrm{slot}}_p G_{pq} \,. \tag{4.23}$$

Defining G_{qq} by

$$G_{qq} = \frac{K_2 f_q^2}{Y^{\mathrm{self}}_q/G_0} \,, \tag{4.24}$$

we obtain the matrix equation

$$G^T V^{\mathrm{slot}} = \frac{K_2}{K_1} V^f \,, \tag{4.25}$$

where $V_q^f = f_q V_q$. The transpose is not present in [30, Eq. (6)], probably because G is symmetric.

To solve the linear system we need to calculate first the right-hand side vector V^f. In [30] two approaches are described to calculate this vector and to resolve the system. The first approach is an iterative procedure where the mode voltages V_q across Y_q^{act} are computed by transmission-line theory from the value of Y_q^{act} in the previous iteration. The slot voltages are then obtained from the linear system as $V^{\text{slot}} = G^{-1}V^f K_2/K_1$ and an update of Y_q^{act} is obtained from the second design equation. The initial values for this procedure are $Y_q^{\text{act}} = Y_q^{\text{self}}$. In the second approach the mode voltages V_q are first explicitly calculated from a recursion relation also obtained from transmission-line theory. We detail the derivation of this recursion relation and demonstrate the calculation of the mode voltages.

The input admittance of a transmission line with admittance Y_0 and load Y_{L}, as illustrated in Figure 4.3, is given by

$$Y_{\text{in}} = Y_0 \, \frac{Y_{\text{L}} \cos\beta\ell + jY_0 \sin\beta\ell}{Y_0 \cos\beta\ell + jY_{\text{L}} \sin\beta\ell}\,, \tag{4.26}$$

where β is the wave number on the transmission line and ℓ is its length. We can employ this expression to calculate the total admittance Y_q^{tot} at the input of the waveguide section up to slot q by recursion. The section can be viewed as the active admittance Y_q^{act} of slot q placed at the terminals of a transmission line, as illustrated in Figure 4.4. The admittance of the transmission line is $Y_0 = \beta_{10}/\omega\mu_0$ of the propagating TE_{10} mode in the waveguide, its length is the distance between slots $q-1$ and q, and its load is Y_{q-1}^{tot}. Consequently, Y_q^{tot} is given by

$$Y_q^{\text{tot}} = Y_q^{\text{act}} + Y_0 \, \frac{Y_{q-1}^{\text{tot}} \cos\beta_{10} d_q + jY_0 \sin\beta_{10} d_q}{Y_0 \cos\beta_{10} d_q + jY_{q-1}^{\text{tot}} \sin\beta_{10} d_q}\,, \quad q \geq 2, \tag{4.27}$$

where $d_q = c_{q,z} - c_{q-1,z}$. The starting value of the recursion is given by

$$Y_1^{\text{tot}} = Y_1^{\text{act}} + Y^{\text{end}}\,, \tag{4.28}$$

where Y^{end} is the load of the waveguide that depends on the type of slotted waveguide array. A traveling-wave array is closed by a matched load for which $Y^{\text{end}} = Y_0$. A resonant array is closed by a short circuit for which $Y^{\text{end}} = -jY_0 \cot\beta_{10} d_1$. Here d_1 is the distance between the short circuit and the centre of the first slot. If d_1 is equal to $\pi/2\beta_{10}$, i.e., a quarter of the guide wavelength, we obtain $Y^{\text{end}} = 0$.

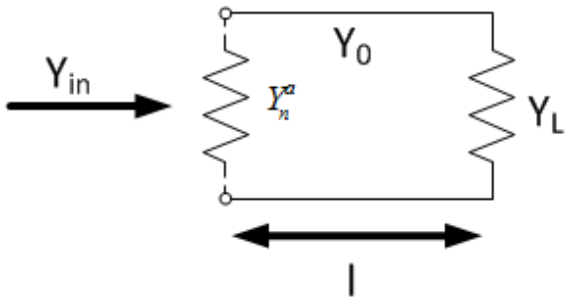

Figure 4.4: Transmission line as in Figure 4.3, but with shunt element Y_q^{act} at its input terminals.

We can write (4.27) in a normalized form as in [30, Eq. (3)],

$$\hat{Y}_q^{\text{tot}} = \hat{Y}_q^{\text{act}} + \frac{\hat{Y}_{q-1}^{\text{tot}} \cos\beta_{10} d_q + j \sin\beta_{10} d_q}{\cos\beta_{10} d_q + j\hat{Y}_{q-1}^{\text{tot}} \sin\beta_{10} d_q}\,, \quad q \geq 2, \tag{4.29}$$

where $\hat{Y}_q^{\text{tot}} = Y_q^{\text{tot}}/Y_0$ and $\hat{Y}_q^{\text{act}} = Y_q^{\text{act}}/Y_0$. The denominator in the second term of the right-hand side indicates that the mode voltages V_q at Y_q^{act} follow also by recursion,

$$V_q = V_{q-1}\left(\cos\beta_{10} d_q + j\hat{Y}_{q-1}^{\text{tot}} \sin\beta_{10} d_q\right)\,, \quad q \geq 2. \tag{4.30}$$

From this relation with q replaced by $q+1$ we can derive a recursion relation for the mode voltages in terms of the slot voltages from which the mode voltages can be resolved explicitly. To derive the recurrence relation we substitute first the expression for $\hat{Y}_q^{\text{tot}}$ given by (4.29) in (4.30) with q replaced by $q+1$,

$$V_{q+1} = V_q \left(\cos\beta_{10}d_{q+1} + j\hat{Y}_q^{\text{tot}} \sin\beta_{10}d_{q+1}\right) =$$
$$= V_q \cos\beta_{10}d_{q+1} + jV_q\hat{Y}_q^{\text{act}} \sin\beta_{10}d_{q+1} + jV_q \frac{\hat{Y}_{q-1}^{\text{tot}} \cos\beta_{10}d_q + j\sin\beta_{10}d_q}{\cos\beta_{10}d_q + j\hat{Y}_{q-1}^{\text{tot}} \sin\beta_{10}d_q} \sin\beta_{10}d_{q+1}\,. \quad (4.31)$$

By (4.30) the denominator of the fraction in the right-hand side equals V_q/V_{q-1}. Moreover, by the first design equation (4.17) we can replace $\hat{Y}_q^{\text{act}}$ by $K_1 f_q V_q^{\text{slot}}/V_q$. Consequently,

$$V_{q+1} = V_q \cos\beta_{10}d_{q+1} + jK_1 f_q V_q^{\text{slot}} \sin\beta_{10}d_{q+1} +$$
$$+ jV_{q-1}\left(\hat{Y}_{q-1}^{\text{tot}} \cos\beta_{10}d_q + j\sin\beta_{10}d_q\right)\sin\beta_{10}d_{q+1}\,. \quad (4.32)$$

By (4.30) we can express $\hat{Y}_{q-1}^{\text{tot}}$ as

$$\hat{Y}_{q-1}^{\text{tot}} = \frac{V_q - V_{q-1}\cos\beta_{10}d_q}{jV_{q-1}\sin\beta_{10}d_q}\,. \quad (4.33)$$

Substituting this expression in (4.32) we obtain

$$V_{q+1} = V_q \cos\beta_{10}d_{q+1}\left(1 + \frac{\cos\beta_{10}d_q}{\cos\beta_{10}d_{q+1}}\frac{\sin\beta_{10}d_{q+1}}{\sin\beta_{10}d_q}\right) + jK_1 f_q V_q^{\text{slot}} \sin\beta_{10}d_{q+1} +$$
$$- V_{q-1}\left(\cos^2\beta_{10}d_q \frac{\sin\beta_{10}d_{q+1}}{\sin\beta_{10}d_q} + \sin\beta_{10}d_q \sin\beta_{10}d_{q+1}\right), \quad (4.34)$$

or

$$V_{q+1} - V_q \cos\beta_{10}d_{q+1}\left(1 + \frac{\tan\beta_{10}d_{q+1}}{\tan\beta_{10}d_q}\right) + V_{q-1}\frac{\sin\beta_{10}d_{q+1}}{\sin\beta_{10}d_q} =$$
$$= jK_1 f_q V_q^{\text{slot}} \sin\beta_{10}d_{q+1}\,, \quad q \geq 2. \quad (4.35)$$

This expression is more general than [30, Eq. (8)], since the spacing between the slots is not necessarily uniform. For constant spacing, (4.35) reduces to [30, Eq. (8)],

$$V_{q+1} - 2V_q \cos\beta_{10}d + V_{q-1} = jK_1 f_q V_q^{\text{slot}} \sin\beta_{10}d\,, \quad q \geq 2, \quad (4.36)$$

where d is the spacing between the slots along the waveguide. By these recurrence relations, the mode voltages V_q with $q \geq 3$ are expressed in V_2 and V_1. We can also express V_2 in terms of V_1. Substituting (4.28) in (4.30) with $q = 2$ and employing the first design equation to replace $\hat{Y}_1^{\text{act}}$ by $K_1 f_1 V_1^{\text{slot}}/V_1$, we obtain

$$V_2 = V_1\left(\cos\beta_{10}d_2 + j\hat{Y}^{\text{end}} \sin\beta_{10}d_2\right) + jK_1 f_1 V_1^{\text{slot}} \sin\beta_{10}d_2 \quad (4.37)$$

where $\hat{Y}^{\text{end}} = \frac{Y^{\text{end}}}{Y_0}$. According to Hamadallah [30, Eq. (10)], the explicit solution for V_q of the recurrence equations (4.36) and (4.37) is given by

$$V_q = V_1\Psi_q + jK_1 \sum_{p=1}^{q-1} f_p V_p^{\text{slot}} \sin(q-p)\beta_{10}d\,, \quad (4.38)$$

where

$$\Psi_q = \cos(q-1)\beta_{10}d + j\hat{Y}^{\text{end}} \sin(q-1)\beta_{10}d\,. \quad (4.39)$$

To demonstrate the validity of this solution, we apply induction. First, for $q = 2$ the solution turns into the relation (4.37). Next, assuming that the solution is valid up to the index q and employing the recurrence relation (4.36) we can write V_{q+1} as

$$V_{q+1} = V_1(2\Psi_q \cos\beta_{10}d - \Psi_{q-1}) + 2jK_1 \sum_{p=1}^{q-1} f_q V_q^{\text{slot}} \sin(q-p)\beta_{10}d \cos\beta_{10}d + \\ - jK_1 \sum_{p=1}^{q-2} f_q V_q^{\text{slot}} \sin(q-1-p)\beta_{10}d + jK_1 f_q V_q^{\text{slot}} \sin\beta_{10}d\,. \quad (4.40)$$

In the second sum we can raise the upper index from $q-2$ to $q-1$, since the $q-1$ term vanishes. Then we can write

$$V_{q+1} = V_1[2\Psi_q \cos\beta_{10}d - \Psi_{q-1}] + \\ + jK_1 \sum_{p=1}^{q-1} f_q V_q^{\text{slot}} [2\sin(q-p)\beta_{10}d \cos\beta_{10}d - \sin(q-1-p)\beta_{10}d] + jK_1 f_q V_q^{\text{slot}} \sin\beta_{10}d\,. \quad (4.41)$$

It can straightforwardly be shown that the two terms between suare brackets are given by

$$\Psi_{q+1} = 2\Psi_q \cos\beta_{10}d - \Psi_{q-1}\,, \quad (4.42)$$

and

$$\sin(q+1-p)\beta_{10}d = 2\sin(q-p)\beta_{10}d \cos\beta_{10}d - \sin(q-1-p)\beta_{10}d\,. \quad (4.43)$$

From the last three equations, (4.38) with q replaced by $q+1$ follows straightforwardly. Thus, we have shown that if the solution is valid up to index q, it is also valid for index $q+1$.

By the explicit solution (4.38) for the mode voltages V_q we can write the components of the vector V^f in the right-hand side of our matrix equation (4.25) as

$$V_q^f = V_1 f_q \Psi_q + jK_1 \sum_{p=1}^{q-1} f_p f_q V_p^{\text{slot}} \sin(q-p)\beta_{10}d = V_1 \Psi_q^f + \frac{K_1}{K_2} \sum_{p=1}^{q-1} \tilde{G}_{pq} V_p^{\text{slot}}\,, \quad (4.44)$$

where $\Psi_q^f = f_q \Psi_q$ and

$$\tilde{G}_{pq} = \begin{cases} jK_2 f_p f_q \sin(q-p)\beta_{10}d, & p < q\,, \\ 0, & p \geq q\,. \end{cases} \quad (4.45)$$

Thus, $\tilde{G}$ is a upper triangular matrix. The matrix form of (4.44) is

$$V^f = V_1 \Psi^f + \frac{K_1}{K_2} \tilde{G}^T V^{\text{slot}}\,. \quad (4.46)$$

Substituting this result in the matrix equation (4.25) we arrive at

$$(G - \tilde{G})^T V^{\text{slot}} = \frac{K_2}{K_1} V_1 \Psi^f \quad (4.47)$$

4.3.4 The Self Coupling

In an internal note [25] Bekers describes a corrected version of the self-coupling expression of Yee [24] in terms of the notation in this thesis. Since Yee's original expression of the junction susceptance is not convergent, we have used the expressions of Oliner [22], [23] to calculate the self coupling of a slot. Oliner describes a derivation of the self admittance of a slot that is displaced

from the centre of the waveguide. He uses variational field expressions and equivalent-circuit considerations [23, Eqs. (9),(10),(11)]. The resulting self-admittance expression is

$$\frac{G_{\mathrm{self},q}}{Y_0} = \frac{\frac{R_{\mathrm{self},q}}{Z_0}}{\left(\frac{R_{\mathrm{self},q}}{Z_0}\right)^2 + \left(\frac{X_{\mathrm{self},q}}{Z_0}\right)^2}, \qquad \frac{B_{\mathrm{self},q}}{Y_0} = \frac{-\frac{X_{\mathrm{self},q}}{Z_0}}{\left(\frac{R_{\mathrm{self},q}}{Z_0}\right)^2 + \left(\frac{X_{\mathrm{self},q}}{Z_0}\right)^2}, \tag{4.48}$$

where,

$$\frac{R_{\mathrm{self},q}}{Z_0} = \frac{G_{c,q}}{Z_0}\left(V_q^{\mathrm{h}}\right)^2, \qquad \frac{X_{\mathrm{self},q}}{Z_0} = \frac{B_{c,q}}{Z_0}\left(V_q^{\mathrm{sh}}\right)^2. \tag{4.49}$$

In (4.49) $\frac{G_{c,q}}{Z_0}$ and $\frac{B_{c,q}}{Z_0}$ are the normalized conductance and normalized susceptance of a centred transverse series slot in the broad wall of a rectangular waveguide. In Oliners derivation V_q^{sh} is the only parameter that depends on the offset of the slot. In our notation V_q^{sh} is given by

$$V_q^{\mathrm{sh}} = \frac{\beta_{10}a}{\pi}\frac{\cos\frac{\pi\ell_q}{a}\left[1-\left(\frac{\beta_{10}\ell_q}{\pi}\right)^2\right]}{\cos\left(\beta_{10}\ell_q\right)\left[1-\left(\frac{2\ell_q}{a}\right)^2\right]}\csc\frac{\pi(c_{q,x}-\frac{a}{2})}{a} \tag{4.50}$$

where $c_{q,x}$ is the x-coordinate of the centre of the slot. The conductance and susceptance of the slot are presented in [23, Eq (1), (2)]. In our notation they are given by

$$\frac{G_{c,q}}{Z_0} = \frac{\frac{1}{N_{\mathrm{jun},q}^2}\left(\frac{\beta_{10,q}}{\beta_{10}}\right)^2\frac{G_{\mathrm{rad},q}}{Y_0}\left(1+\cot^2\beta_{10,q}t\right)}{\left(\frac{G_{\mathrm{rad},q}}{Y_0}\right)^2+\left(\frac{\beta_{10,q}}{\beta_{10}}\cot\beta_{10,q}t-\frac{B_{\mathrm{rad},q}}{Y_0}\right)^2}, \tag{4.51}$$

$$\begin{aligned}\frac{B_{e,q}}{Z_0} = \frac{B_{\mathrm{jun},q}}{Y_0} + \frac{1}{N_{\mathrm{jun},q}^2}\frac{\beta_{10,q}}{\beta_{10}}\times \\ \times\frac{\frac{B_{\mathrm{rad},q}}{Y_0}\frac{\beta_{10,q}}{\beta_{10}}\left(\cot^2\beta_{10,q}t-1\right)+\left(\left(\frac{\beta_{10,q}}{\beta_{10}}\right)^2-\left(\frac{B_{\mathrm{rad},q}}{Y_0}\right)^2-\left(\frac{G_{\mathrm{rad},q}}{Y_0}\right)^2\right)\cot\beta_{10,q}t}{\left(\frac{G_{\mathrm{rad},q}}{Y_0}\right)^2+\left(\frac{\beta_{10,q}}{\beta_{10}}\cot\beta_{10,q}t-\frac{B_{\mathrm{rad},q}}{Y_0}\right)^2},\end{aligned} \tag{4.52}$$

The parameter t is the thickness of the waveguide wall. If the thickness approaches zero, (4.51) and (4.52) reduce to

$$\frac{G_{c,q}}{Z_0} = \frac{1}{N_{\mathrm{jun},q}^2}\frac{G_{\mathrm{rad},q}}{Y_0}, \tag{4.53}$$

$$\frac{B_{c,q}}{Z_0} = \frac{B_{\mathrm{jun},q}}{Y_0} + \frac{1}{N_{\mathrm{jun},q}^2}\frac{B_{\mathrm{rad},q}}{Y_0}, \tag{4.54}$$

where $N_{\mathrm{jun},q}^2$ is a ratio between the ongoing waveguide and the junction with the half space of the slot. The parameter $\frac{1}{N_{\mathrm{jun},q}^2}$ is given by

$$\frac{1}{N_{\mathrm{jun},q}^2} = \frac{ab}{4\ell_q w_q}\left(\frac{\pi}{4}\frac{1-\left(\frac{2\ell_q}{a}\right)^2}{\cos\frac{\pi\ell_q}{a}}\right)^2. \tag{4.55}$$

Since Oliners accounts for the slot offset by a separate factor, namely V_q^{sh}, his expression for the susceptance differs from that of Yee and Bekers and, is given by

$$\frac{B_{\mathrm{jun},q}}{Y_0} = \frac{1}{2}\frac{B_{t,q}}{Y_0} + \frac{\beta_{10}b}{\pi}\left(\log 2 + \frac{\pi}{6} + \frac{2w_q}{b} + \frac{3}{2}\left(\frac{\beta_{10}b}{2\pi}\right)^2\right), \tag{4.56}$$

where $\frac{B_{t,q}}{Y_0}$ is given by

$$\frac{B_{t,q}}{Y_0} = \frac{2b\beta_{10}}{\pi}\left(\log\left(\csc\frac{\pi w_q}{b}\right) + \frac{1}{2}\left(\frac{b\beta_{10}}{2\pi}\right)^2\left(\cos\frac{\pi w_q}{2b}\right)^4\right) - \frac{2b\beta_{10}}{\pi}\left(\frac{2\pi}{\beta_{10}\lambda_{gs}}\right)^2\left(\frac{\left(1-\left(\frac{2\ell_q}{a}\right)^2\right)\cos\frac{3\pi\ell_q}{a}}{\left(1-9\left(\frac{2\ell_q}{a}\right)^2\right)\cos\frac{\pi\ell_q}{a}}\right)^2\left(1+\left(\frac{\pi w_q}{\lambda_{gs}}\right)^2\right)\log\frac{2\lambda_{gs}}{\pi w_q\gamma'}. \quad (4.57)$$

In this expression γ' is given by $\gamma' = e^{\gamma} \approx 1.781$, where γ is the exponent of the constant of Euler. furthermore λ_{gs} is given by

$$\lambda_{gs} = \left|\frac{\lambda}{\sqrt{1-\left(\frac{3\lambda}{2a}\right)^2}}\right|. \quad (4.58)$$

The quantities $\frac{G_{\mathrm{rad},q}}{Y_0}$ and $\frac{B_{\mathrm{rad},q}}{Y_0}$ in (4.51) and (4.52) are given by [23, Eqs. (5),(6)], [25, Eqs.(66),(67)]

$$\frac{G^{\mathrm{rad}}}{Y_0} = \frac{256\pi\ell_q w_q}{3\beta_{10}\lambda^3}\left(1-0.374\left(\frac{2\ell_q}{\lambda}\right)^2+0.130\left(\frac{2\ell_q}{\lambda}\right)^4\right), \quad (4.59)$$

and

$$\frac{B^{\mathrm{rad}}}{Y_0} = \frac{8w_q\pi}{\beta_{10}\lambda^2}\left(\left(\frac{\beta_{10,q}}{\beta_{10}}\right)^2\left(C_{1,q}+\frac{3}{2}-\gamma-\ln(|\beta_{10}|w_q)\right) + \frac{\sin 2k\ell_q}{2k\ell_q} + C_{2,q}\left(1+\left(\frac{\lambda}{4\ell_q}\right)^2\right) - \frac{2w_q}{3\ell_q}\left(\frac{\lambda}{4\ell_q}\right)^2\right). \quad (4.60)$$

With these adapted expressions it is possible to calculate the self admittance of a single slot on a waveguide section. To validate the expressions, we insert the parameters that Oliner used in [23, Fig.6]. These parameters are given in Table 4.1.

Table 4.1: Parameters used by Oliner to validate the calculated self-admittance in the expressions in (4.48)

Variable	Value
Frequency (f)	9.375 GHz
Waveguide width (a)	0.0229 m
Waveguide hight (b)	0.0102 m
Slot offset from the centre	0.0019 m
Slot width (2w)	0.0016 m
Thickness of the waveguide wall (t)	0.0013 m

Figure 4.5 shows the resulting susceptance and conductance as functions of four times the slot length over the wavelength. The two curves in each plot concern the results with and without waveguide thickness included. The curves in Figure 4.5 match reasonably with the curve presented in [23, Fig. 16]. The magnitudes of the susceptance and admittance in our plots are approximately $0.039Y_0$ and $0.075Y_0$, while Oliner obtains values of approximately $0.040Y_0$ and $0.083Y_0$. The differences between these magnitudes can be compensated by setting the waveguide width in our calculation to 99% of its original value. This difference of widht may be within manufacturing tolerances. moreover note that Oliner's approximation and measurement in [23, Fig. 16] show slight amplitude differences as well as frequency shifts.

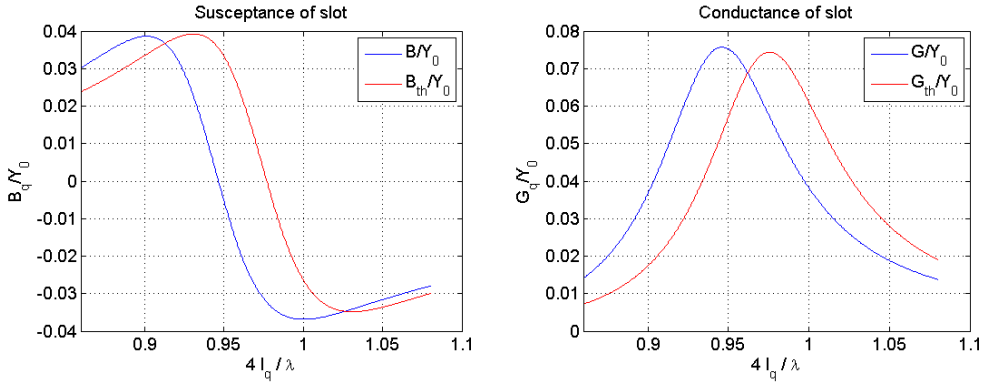

(a) (b)

Figure 4.5: The susceptance(a) and conductance(b) as function of two times the slot length over the wavelength, using the parameters given in Table 4.1. The subscript th indicates that the waveguide thickness of 0.0013m is included.

The expressions of Yee [24] have been corrected by Bekers in [25]. Their expression to calculate the self impedance is

$$\frac{Z_q^{\text{self}}}{Z_0} = \frac{2\ell_q w_q}{A_q}\left(\frac{Y_q^{\text{rad}}}{Y_0} + j\frac{B_q^{\text{jun}}}{Y_0}\right), \tag{4.61}$$

where $\frac{Y_q^{\text{rad}}}{Y_0}$ is given by $\frac{Y_q^{\text{rad}}}{Y_0} = \frac{G_q^{\text{rad}}}{Y_0} + j\frac{B_q^{\text{rad}}}{Y_0}$. Bekers derived an expression for $\frac{B_q^{\text{jun}}}{Y_0}$ which is given by

$$\frac{B_q^{\text{jun}}}{Y_0} = \frac{8w_q}{\omega\mu_0 ab} \sum_{\substack{m,n=0 \\ (m,n)\neq(0,0)}}^{\infty} \frac{1}{\varepsilon_m \varepsilon_n} \cos^2\left(\frac{m\pi c_{q,x}}{a}\right) \times$$

$$\times \operatorname{sinc}^2\left(\frac{m\pi w_q}{a}\right) \operatorname{Im}\left[j(Q_{1,q}(m,n) + Q_{2,q}(m,n))\right], \tag{4.62}$$

where

$$\varepsilon_n = \begin{cases} 1, & n \neq 0\,, \\ 2, & n = 0\,. \end{cases} \tag{4.63}$$

The sinc function is defined by $\frac{\sin x}{x}$ and $c_{q,x}$ indicates the x coordinate of the slot centre. The functions $Q_{1,q}$ and $Q_{2,q}$ are given by

$$Q_{1,q}(m,n) = \frac{\beta_{10,q}^2}{(\pi/2\ell_q) - \beta_{mn}^2}, \tag{4.64}$$

$$Q_{2,q}(m,n) = 2\left(\frac{\pi}{2\ell_q}\right)^2 \frac{k^2 - \beta_{mn}^2}{((\pi/2\ell_q)^2 - \beta_{mn^2})^2} \frac{1 + \exp(-2j\beta_{mn}\ell_q)}{2j\beta_{mn}\ell_q}, \tag{4.65}$$

where β_{mn} is given by

$$\alpha = k^2 - \left(\frac{m\pi}{a}\right)^2 - \left(\frac{n\pi}{b}\right)^2,$$

$$\beta_{mn} = \begin{cases} \sqrt{\alpha}, & \alpha \geq 0\,, \\ -j\sqrt{-\alpha}, & \alpha < 0\,. \end{cases}$$

In Yee's expression for $\frac{B_q^{\text{jun}}}{Y_0}$ the series is not convergent. This has been traced back in [25] to an error in the denominator of one of the fractions of $Q_{2,q}$, which needed to be squared. Besides,

Yee's expression suffers from a dimensional problem in $Q_{2,q}$, where the length scale ℓ_q is missing in the exponent and the denominator. The results of the corrected expressions of Yee are shown in Figure 4.6.

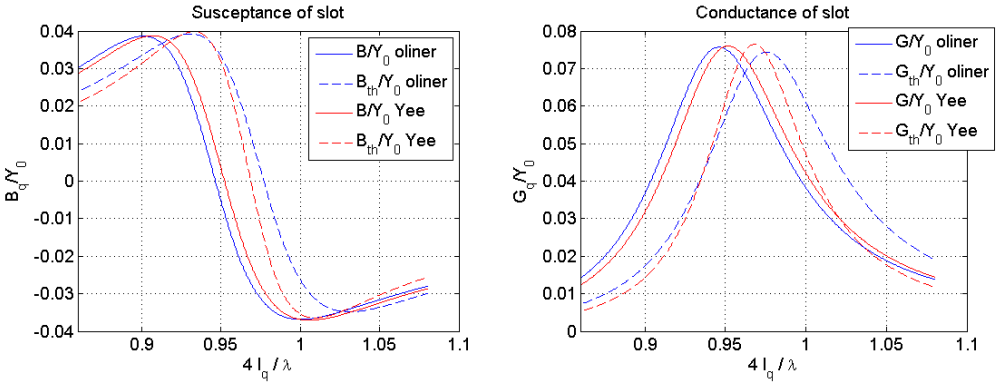

(a) (b)

Figure 4.6: The susceptance (a) and conductance (b) as function of two times the slot length over the wavelength, calculated with the parameters given in Table 4.1 with Yee's and oliners expressions. The subscript th indicates that the thickness is included.

The obtained expression for the self coupling and the linear system for the mutual coupling can now be used for an implementation of a full model of a single slotted waveguide array. In the next chapter the steps for the implementation are detailed

Chapter 5

Implementation and Results

In this chapter we describe first the implementation for the computation of the slot voltages based on the theory in the previous chapter. Next we describe the derivation of the expression for the far-field radiation patterns which are composed of the slot voltages. This leads to a code capable of computing accurate far field patterns rapidly. We validate our implementation for slot voltages and patterns using two test cases. The first test case concerns resonant and travelling wave arrays of 7 slots as in [30]. The second test case concerns resonant array of 40 slots. The result of the implementation and validation will be a code capable of calculating the coupling coefficients, slot voltages and the normalized far field radiation pattern for travelling wave or resonant slotted waveguide arrays with uniform or non-uniform slot offsets.

5.1 Implementation

The implementation of the matrix system in (4.47) is divided in three parts for re-usability and easy manipulation of parameters. The first part is the generation of matrix G. Matrix G can be generated for one or more array settings simultaneously. The second part is the generation of vectors Ψ in the right-hand side of 4.47 for one or more array settings. In the third part the system of equations 4.47 is constructed and the solution is computed by standard algorithms in Matlab. For the generation of the matrix G and vector Ψ, variables such as K_1 and K_2 need to be calculated, these variable are later again required for the calculation of the slot voltages. Therefore these variables are stored for later use.

We focus on the G matrix first. The diagonal components of the matrix represent the self-coupling as described in (4.24), where we calculate Y_q^{self} as in 4.3.4. The expression for the off diagonal components is given by [25, Eq (56)]

$$G_{pq} = \frac{\ell_p k_0}{\pi}\left[U_{1,pq} + U_{2,pq} - \frac{1}{4k_0^2\ell_p\ell_q}(U_{1,pq} - U_{2,pq})\right], \tag{5.1}$$

with

$$U_{i,pq} = \int_{-\ell_p-\ell_q}^{\ell_p+\ell_q} F_{pq}(\zeta)W_{i,pq}(\zeta)d\zeta, \tag{5.2}$$

where

$$F_{pq}(\zeta) = \frac{\exp(-jk_0R_{pq}(\zeta,0))}{R_{pq}(\zeta,0)}. \tag{5.3}$$

The distance between the slot centres, is indicated by R_{pq}. The functions W_{pq} indicate the convolution between the currents of the two slots.

In the software it numerical integration is used to evaluate the integrals (5.2). The technique that is used to evaluate the integral is the Simpson rule. On an interval the Simpson rule defines 3

points: the start of the interval, the centre of the interval and, the end of the interval. The weight factors $1, 4, 1$ are assigned to the points and multiplied with $\frac{1}{3}$ times the spacing between the points. Consequently, the simpson rule is exact for polynomials up to degree two. For increased accuracy we apply the Simpson rule to subintervals of the integration in 5.2. To avoid evaluating the integrand twice at each end point of these intervals we cascade the separate simpson rules to a single rule with weight factors $1, 4, 2, 4, 2, 4, 2, \ldots, 1$.

The vector Ψ is generated as in (4.39). The termination of the waveguide array, Y^{end}, depends on the array configuration. If the array is a travelling wave array the waveguide is terminated with a matched load, $Y^{\text{end}} = Y_0$. For a standing wave array the waveguide is terminated with a short circuit, $Y^{\text{end}} = -jY_0 \cot \beta_{10} d_1$, where d_1 is the distance from the short circuit of the waveguide to the centre of the first slot. In the previously derived models the excitation takes place at the end of the waveguide. We also consider waveguides where the excitation takes place in the centre. In that case we can calculate the vector Ψ by applying (4.39)to both sides of the waveguide. When the feed is placed at another place in the array, the standing-wave case needs to be reconsidered since difference in path length can cause destructive addition between the reflected waves from two end of the waveguide.

The final calculation is done in the function where V^{slot} is generated. The first step is the calculation of the square upper triangular matrix $\tilde{G}$, which is defined in (4.45). To implement this matrix a "*for loop*" can be used. However the Matlab environment is more efficient when using matrix calculations. The functions f_p and f_q of $\tilde{G}$ can be generated as vectors. The sine only depends on the difference of the row and column indices p and q. Therefore, on each (co)diagonal, the matrix elements are identical. Hence, $\sin(p-q)\beta_{10} d$ can be represented as a Toeplitz matrix, for which the standard implementation of Matlab is used.

The other components required for the matrix system (4.47) are already available from the calculation of G. To solve the system, $G - \tilde{G}$ needs to be inverted. In Matlab we use the "\" commando, which employs Gaussian elimination to find the inversion of the system instead of calculating the inverse of the matrix first.

5.2 Antenna-Pattern Calculation

Having computed the solution of the matrix system (4.47) by the implementation described in the previous section, we can compute the far-field of a slotted-waveguide array. In this section we derive the expressions for the magnetic far-field and related quantities such as the radiation intensity and the directivity.

The total magnetic field of an array of longitudinal slots is described by the sum of the contributions of the slots,

$$\boldsymbol{H} = \sum_{q=1}^{Q} \boldsymbol{H}_q \,, \tag{5.4}$$

where the contribution $\vec{H}_q$ of a slot is given by

$$\boldsymbol{H}_q = -j\omega\varepsilon_0 \left(1 + \frac{1}{k_0^2} \operatorname{grad} \operatorname{div}\right) \boldsymbol{F}_q \,. \tag{5.5}$$

In this equation the electric vector potential $\boldsymbol{F}_q$ is defined by

$$\boldsymbol{F}_q(\boldsymbol{x}) = \frac{1}{4\pi} \int_{-\ell_q}^{\ell_q} \int_{-w_q}^{w_q} \frac{\exp(-jk_0 \|\boldsymbol{x} - \boldsymbol{x}_{S_q}(\zeta,\xi)\|_2)}{\|\boldsymbol{x} - \boldsymbol{x}_{S_q}(\zeta,\xi)\|_2)} M_q(\zeta) d\xi d\zeta \, \boldsymbol{i}_z \,. \tag{5.6}$$

where $M_q$is the width-averaged magnetic current at the slot,

$$M_q(\zeta) = \frac{V_q^{\text{slot}}}{w_q} \cos\left(\frac{\pi\zeta}{2\ell_q}\right). \tag{5.7}$$

We express $\boldsymbol{x}$ in the spherical coordinate system $\{\boldsymbol{i}_r, \boldsymbol{i}_\theta, \boldsymbol{i}_\phi\}$ defined by

$$\begin{aligned} \boldsymbol{i}_r(\theta,\phi) &= \sin\theta\cos\phi\,\boldsymbol{i}_z + \sin\theta\sin\phi\,\boldsymbol{i}_x + \cos\theta\,\boldsymbol{i}_y, && (5.8)\\ \boldsymbol{i}_\theta(\theta,\phi) &= \cos\theta\cos\phi\,\boldsymbol{i}_z + \cos\theta\sin\phi\,\boldsymbol{i}_x - \sin\theta\,\boldsymbol{i}_y, && (5.9)\\ \boldsymbol{i}_\phi(\theta,\phi) &= -\sin\phi\,\boldsymbol{i}_z + \cos\phi\,\boldsymbol{i}_x. && (5.10) \end{aligned}$$

This system is derived from the classical coordinate system by applying the permutation $(x, y, z) \to (z, x, y)$. We set $\boldsymbol{x} = b\,\boldsymbol{i}_y + r\,\boldsymbol{i}_r$ such that r is the distance from a point in $\boldsymbol{x}$ in the far-field to a point on the top of the waveguide, where the subarray is located. Then,

$$\|\boldsymbol{x} - \boldsymbol{x}_{S_q}\|_2 = \sqrt{r^2 - 2r(\boldsymbol{i}_r(\theta,\phi)\cdot(\boldsymbol{x}_{S_q}(\zeta,\xi) - b\,\boldsymbol{i}_y)) + |\boldsymbol{x}_{S_q}(\zeta,\xi) - b\,\boldsymbol{i}_y|^2}\,. \tag{5.11}$$

By a similar dimension analysis as described in [31, Appendix C] we need to neglect terms of order $O(L^2/r^2)$ in the phase term of (5.6) and the terms of $O((L+1/k)/r)$ in all other terms, where is the characteristic size of the array. Then,

$$\boldsymbol{H}_q = -j\omega\varepsilon_0\,(F_{q,\theta}\,\boldsymbol{i}_\theta + F_{q,\phi}\,\boldsymbol{i}_\phi) \tag{5.12}$$

and

$$\boldsymbol{F}_q(\boldsymbol{x}) = \frac{e^{-jk_0 r}}{4\pi r}\int_{-\ell_q}^{\ell_q}\int_{-w_q}^{w_q} e^{jk_0(\boldsymbol{i}_r(\theta,\phi)\cdot(\boldsymbol{x}_{S_q}(\zeta,\xi) - b\,\boldsymbol{i}_y))} M_q(\zeta)d\xi d\zeta\,. \tag{5.13}$$

The vector $\boldsymbol{i}_z$ needs to be expressed in $\{\boldsymbol{i}_r, \boldsymbol{i}_\theta, \boldsymbol{i}_\phi\}$. To this end we multiply (5.8) by $\sin\theta$ and (5.9) by $\cos\theta$, and we add the results . Then,

$$\sin\theta\,\boldsymbol{i}_r + \cos\theta\,\boldsymbol{i}_\theta = \cos\phi\,\boldsymbol{i}_z + \sin\phi\,\boldsymbol{i}_x\,. \tag{5.14}$$

Multiplying this equation by $\cos\phi$ and (5.10) by $-\sin\phi$, and adding the results, we obtain

$$\boldsymbol{i}_z = \cos\phi\sin\theta + \cos\phi\cos\theta\,\boldsymbol{i}_\theta - \sin\phi\,\boldsymbol{i}_\phi\,. \tag{5.15}$$

Consequently,

$$F_{q,\left\{\begin{smallmatrix}\theta\\ \phi\end{smallmatrix}\right\}}(r,\theta,\phi) = \begin{Bmatrix}\cos\theta\cos\phi\\ -\sin\phi\end{Bmatrix} F_q(r,\theta,\phi) \tag{5.16}$$

where

$$F_q(p,\theta,\phi) = \frac{e^{-jk_0 r}}{4\pi r} e^{jk_0(c_{q,z}\sin\theta\cos\phi + c_{q,x}\sin\theta\sin\phi)} \times \\ \times \int_{-\ell_q}^{\ell_q} e^{jk_0\zeta\sin\theta\cos\phi} M_q(\zeta)d\zeta \int_{-w_q}^{w_q} e^{jk_0\xi\sin\theta\sin\phi} d\xi\,. \tag{5.17}$$

Here we have used that the slot is placed in the upper waveguide wall, such that $c_{q,y} = b$. Thus,

$$\boldsymbol{i}_{S_q}(\zeta,\xi) - b\,\boldsymbol{i}_y = \boldsymbol{c}_q + \zeta\,\boldsymbol{i}_\zeta + \xi\,\boldsymbol{i}_\xi - b\,\boldsymbol{i}_y = \boldsymbol{c}_q + \zeta\,\boldsymbol{i}_z + \xi\,\boldsymbol{i}_x - b\,\boldsymbol{i}_y = \\ = (\boldsymbol{c}_{q,x} + \xi)\,\boldsymbol{i}_x + (\boldsymbol{c}_{q,z} + \zeta)\,\boldsymbol{i}_z\,. \tag{5.18}$$

Neglecting terms of $O(k_0^2 w_q^2)$ we can approximate the integral with respect to ξ by $2w_q$. Substituting the magnetic current of the slot (5.7) for the integral with respect to ζ in (5.17), we derive

$$\int_{-\ell_q}^{\ell_q} e^{jk_i\zeta\sin\theta\cos\phi} M_q(\zeta)d\zeta = \frac{V_q^{\text{slot}}}{2w_q}\int_{-\ell_q}^{\ell_q}\cos(k_0\sin\theta\cos\phi)\cos\left(\frac{\pi\zeta}{2\ell_q}\right)d\zeta. \tag{5.19}$$

Using a trigonometric identity the integral turns into

$$\int_{-\ell_q}^{\ell_q} e^{jk_i\zeta\sin\theta\cos\phi} M_q(\zeta)d\zeta = \frac{V_q^{\text{slot}}}{2w_q}\int_{-\ell_q}^{\ell_q}\left[\cos\left(\left(\kappa+\frac{\pi}{2\ell_q}\right)\zeta\right)+\cos\left(\frac{\pi\zeta}{2\ell_q}\right)\right] \tag{5.20}$$

where $\kappa = k_0\sin\theta\cos\phi$. Calculating the integral we obtain

$$\int_{-\ell_q}^{\ell_q} e^{jk_i\zeta\sin\theta\cos\phi} M_q(\zeta)d\zeta = -\frac{V_q^{\text{slot}}}{w_q\ell_q}\frac{\pi\cos\kappa\ell_q}{\kappa^2-\left(\frac{\pi}{2\ell_q}\right)^2}\,. \tag{5.21}$$

Substituting the result in (5.17) we obtain

$$F_q(p,\theta,\phi) = -\frac{V_q^{\text{slot}}}{2\ell_q}\frac{e^{-jkr}}{r}e^{jk_0(c_{q,z}\sin\theta\cos\phi+c_{q,x}\sin\theta\sin\phi)}\frac{\cos\kappa\ell_q}{\kappa^2-\left(\frac{\pi}{2\ell_q}\right)^2}\,. \tag{5.22}$$

By (5.4), (5.12),(5.16), and (5.22) we have specified the magnetic far-field. The relation between the electric field and magnetic field in the far-field region is given by $\boldsymbol{H} = \boldsymbol{i}_r\times\boldsymbol{E}/\eta_0$ [31, Appendix C].since $\boldsymbol{i}_r\times(\boldsymbol{i}_r\times\boldsymbol{E}) = (\boldsymbol{i}_r\cdot\boldsymbol{E})\,\boldsymbol{i}_r - \boldsymbol{E}$ and since $\boldsymbol{i}_r\cdot\boldsymbol{E} = 0$ we have

$$\boldsymbol{E} = -\boldsymbol{i}_r\times\eta_0\boldsymbol{H}. \tag{5.23}$$

To calculate the total radiated power in the far-field we need to calculate the time-average pointing vector $\boldsymbol{S} = \text{Re}(\boldsymbol{E}\times\boldsymbol{H}^*)/2$. By using (5.23) we derive

$$\boldsymbol{S} = \text{Re}((-\boldsymbol{i}_r\times\eta_0\boldsymbol{H})\times\boldsymbol{H})/2 = \eta_0(\boldsymbol{H}\cdot\boldsymbol{H}^*)\boldsymbol{i}_r/2\,. \tag{5.24}$$

The total radiated power of an array in a half space is the total flux of $\boldsymbol{S}$ over half a sphere with radius r,

$$P^{\text{rad}} = \int_0^{2\pi}\int_0^{\frac{\pi}{2}}(\boldsymbol{S}\cdot\boldsymbol{i}_r)r^2\sin\theta\,d\theta d\phi = \int_0^{2\pi}\int_0^{\frac{\pi}{2}}U(\theta,\phi)\sin\theta d\theta d\phi\,, \tag{5.25}$$

where $U(\theta,\phi) = (\boldsymbol{S}\cdot\boldsymbol{i}_r)r^2 = \eta_0 r^2(\boldsymbol{H}\cdot\boldsymbol{H}^*)/2$ is the radiation intensity. The directivity is given by [15, Eq. (2-16)],

$$D = \frac{4\pi U(\theta,\phi)}{P^{\text{rad}}}\,. \tag{5.26}$$

5.3 Antenna Test Cases

5.3.1 Test Case 1: Traveling-Wave and Resonant Arrays of Seven Slots

In [30] Hamadallah describes a resonant array of seven slots on a WR62 waveguide. We employ his geometry to validate our implementation for both traveling-wave and resonant slotted-waveguide arrays. The parameters used for the validation are listed in Table 5.1. We note that Hamadallah states that $d = \lambda/2$, but since $\lambda_g = \frac{\lambda_0}{\sqrt{1-(\lambda_0/(2a))^2}} = 0.029$ m for 14.03GHz, Hamadallah's statement should be $d = \lambda_g/2$.

For a resonant array Hamadallah plots the measured self conductance and self susceptance in [30, Fig. 4] as a function of frequency. We have calculated these quantities by the expressions of Oliner and Yee as described in Section 4.3.4. Our results for the normalized conductance in Figure 5.1b show a peak of 0.14 at about 14 GHz. This peak corresponds to the maximum listed by Hamadallah. We note that Hamadallah uses this value to normalise his results for the conductance and susceptance in [30, Fig. 4].

Table 5.1: Parameters used by Hamadallah [30] for a slotted waveguide array of seven slots.

Variable	Value
Frequency	14.03 GHz
Waveguide width (a)	0.0158 m
Waveguide hight (b)	0.0078994 m
Slot offset from the centre	0.0021 m
Slot width (2w)	0.001 m
Slot length(2l)	0.01 m
Thickness of the waveguide wall (t)	0.0013 m

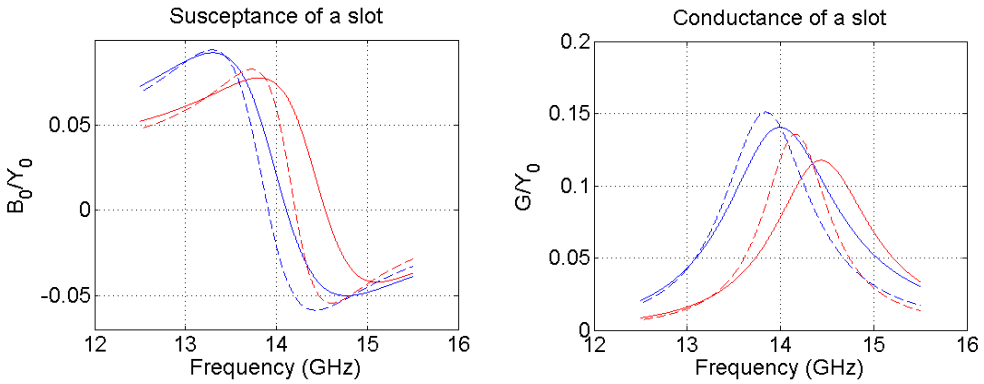

(a) (b)

Figure 5.1: The susceptance (a) and conductance (b) as function of frequency, calculated with the parameters given in Table 5.1 by Yee's expressions (dashed curves) and Oliner's expressions (solid curves). The red lines indicate that the thickness is included, blue lines indicate a thickness of 0.

To validate our moment and far-field code, we compute the radiation intensity in the far-field for the same frequencies as Hamadallah uses in his paper. In Figure 5.2, the curves are shown for the cases with mutual coupling and without mutual coupling, where we normalize the intensity on the maximum of the case without mutual coupling. The difference between the curve with mutual coupling and without mutual coupling is about 0.2 dB for 14.03 GHz, i.e., the frequency for which the array is designed. Below this frequency, the curve with mutual coupling is below the one without mutual coupling as can be observed from Figures 5.2a and 5.2b. This observation can be explained by the destructive behaviour of the coupling. However, above the design frequency the curve with mutual coupling is above the curve without mutual coupling.

At this stage of our research we decided to first verify the expressions for the mutual coupling as derived in [25]. To this end we also implemented Elliott's expression for the matrix components G_{pq} as given by [26, Eq. 30]. Elliott uses a double integral to calculate these components, while in our case the integral is transformed into two single integrals. We calculate the double integral of Elliott using the 2D Simpson rule. The results for the radiation intensity obtained by Elliott's expression compared to our expression are given in Figure 5.3. We observe that there is hardly any difference between the solid and dashed blue curves which represent the results with mutual coupling for our and Elliott's expressions, respectively. To quantify the difference between Elliott's and our expressions we also calculated the relative difference between the two corresponding moment matrices. Figure 5.4a shows the coupling matrix obtained by our expressions and Figure 5.4b shows this relative difference. The largest differences occur for the nearest neighbour coupling on the first co-diagonal, but are not greater than 10^{-6}.

From the previous analysis we conclude that our expressions for the mutual coupling seem to be correct. We thus tried to find a physical explanation for the observed constructive addition of the

coupling. A possible explanation is in the coupling mechanism itself. Power that is transfered from one slot to another by mutual coupling can also be reradiated. Most probably this phenomenon occurs particularly for higher frequencies, since the mode in the slot (interpreted as stub guide) turns from an evanescent mode into a propagating one.

The slot voltages corresponding to the frequencies in Figure 5.3 are given in Figure 5.4c. These voltages are calculated for a prescribed mode voltage V_1 of 1 V at the waveguide section that contains the slot next to the load. Note that, while the first slot is located next to the load, the seventh slot is located next to the source.

5.3.2 Test Case 2: A Traveling-Wave Array of 40 Slots with Varying Offsets

As a second test case we consider a traveling-wave array of 40 slots. The parameters of this test case are presented in Table 5.2. The slot offsets are represented in Figure 5.5. We recall that in our theory the slots are indexed starting from the slot closest to the load. For the waveguide in Figure 5.5, the load is located at the right, where the slots have the largest offset. Consequently, with reference to this figure, we index the slots from right to left.

Although the slot offsets appear in Figure 5.5 as being large towards the end of the waveguide, their maximum magnitude is only about 10% of the waveguide width a. On the other hand, the electromagnetic effect of the varying slot offsets is relatively large as we will illustrate. To this end, we consider also the same array but with a uniform slot offset of 0.4 mm, which is the smallest offset in the array with varying offsets. First, we show the moment-matrix components of the array with varying offsets at an operating frequency of 9.41 GHz. Although the coupling coefficients of the first few slots show some variation, this is not visible in the colors of Figure 5.6a due to the scale of a few tens of dB. The same is valid for the comparison of the coupling coefficients of specific slots as shown in Figure 5.6b. However a closer look reveals differences of about 0.25 dB between the self coupling of the first and 40th slot as is illustrated by the markers in the figure. A better insight in the variation of the coupling coefficients of the array with varying offsets can be obtained by plotting their relative difference with the coupling coefficients of the array with uniform offsets, as we have done in Figure 5.6c. This figure shows clearly varying differences between the components of the two moment matrices along both the diagonal and all co-diagonals.

Running our moment code at three different frequencies (9, 9.41, and 10 GHz) and for the cases with varying and uniform offsets, we obtain the slot voltages as shown in 5.7. For all six considered cases, the array is a traveling-wave array and mutual coupling is included. The cases with varying offsets show higher slot voltages compared to the uniform offsets. The largest differences in slot voltages occur at 9.41 GHz, i.e., the frequency for which the array is designed. Thus, as we observed at moment-matrix level, there are substantial differences between the cases with varying and uniform offsets.

Next to the preceding comparison of varying and uniform offsets, we have made two additional comparisons. In the first one we compare the cases with and without mutual coupling for the traveling-wave array with varying offsets. As Figure 5.8a shows, the effect of the mutual coupling is largest at the frequency for which the array is designed. At the other frequencies the differences are smaller, but the total voltages are also smaller at those frequencies.

In the second comparison we compare a resonant array and a traveling-wave array, both with varying offsets and with mutual coupling included. For the resonant array, the distance between the matched load and the nearest slot is 0.029 mm. Figure 5.8b shows that, in particular at the design frequency, the traveling-wave array results in higher slot voltages than the resonant array. In this respect, we note that for a standing-wave array, uniform offsets are more suitable, because the standing wave will result in slot voltages that have a certain level of symmetry along the waveguide. For all three frequencies in Figure 5.8b we also observe clearly the standing-wave nature of the slot voltages.

With our far-field code we calculate the radiation intensities for the traveling-wave array at three different frequencies. We consider both uniform and varying offsets, and we consider the

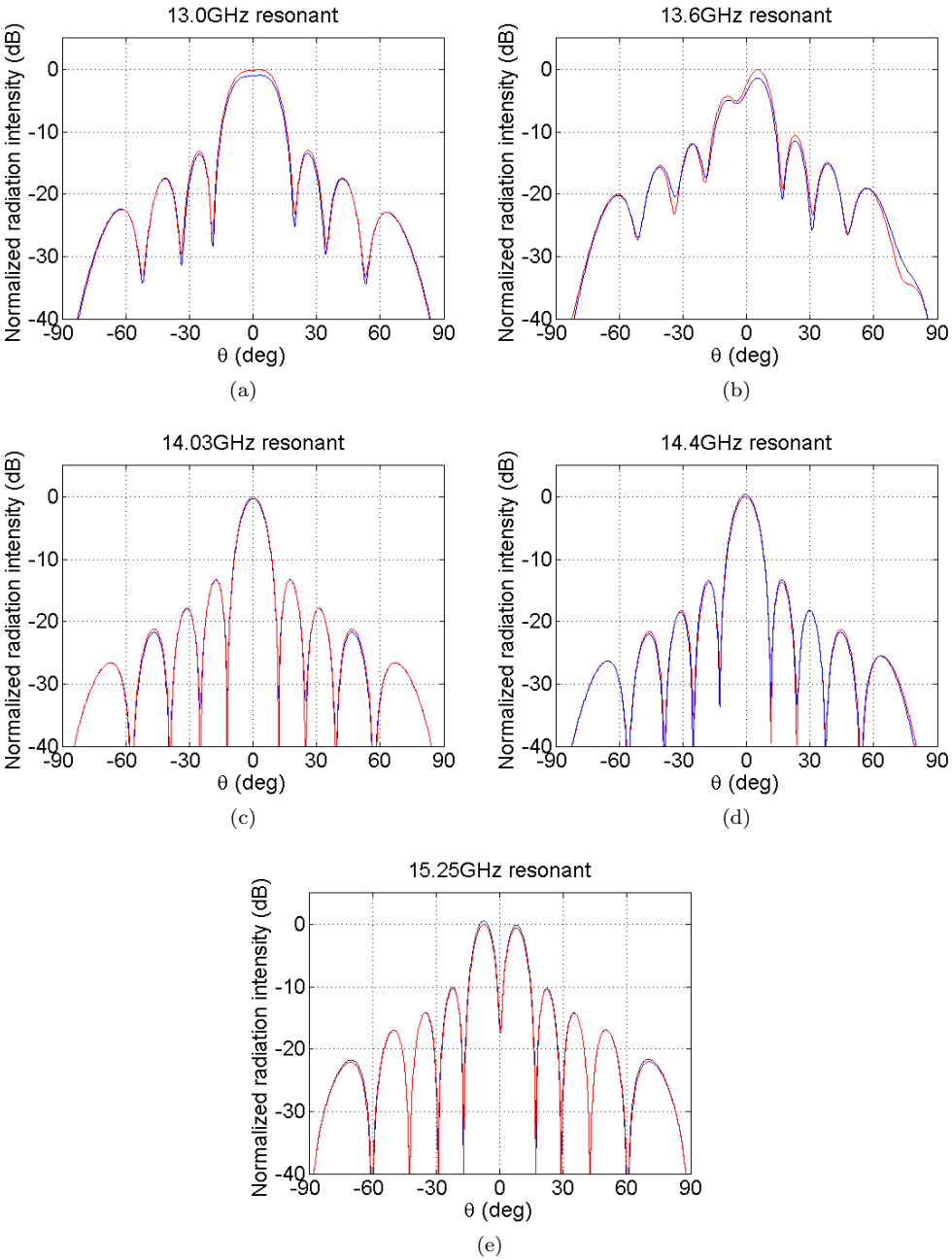

Figure 5.2: The normalised radiation intensity in the far-field plane $\phi = 0$ for the frequencies used in [30] and the parameters listed in 5.1. Blue curves: without mutual coupling. Red curves: with mutual coupling. Normalization: the maximum intensity without mutual coupling.

cases with and without mutual coupling. Figure 5.9a shows that the far-field antenna pattern at 9 GHz has large side lobes near grazing. The main beam is squinted towards approximately 10 degrees and a side lobe of -12 dB is present at -70 degrees. Figure 5.9b shows that at 9.41 GHz the side lobe levels are lower near grazing and there is less squint. The remaining few degrees of squint match the results obtained for such an array by an internal code of TNO that ignores mutual coupling. At 10 GHz the beam is squinted the other side as can be seen in Figure 5.9c.

To investigate the effect of mutual coupling, the results in Figure 5.9 are not very suitable.

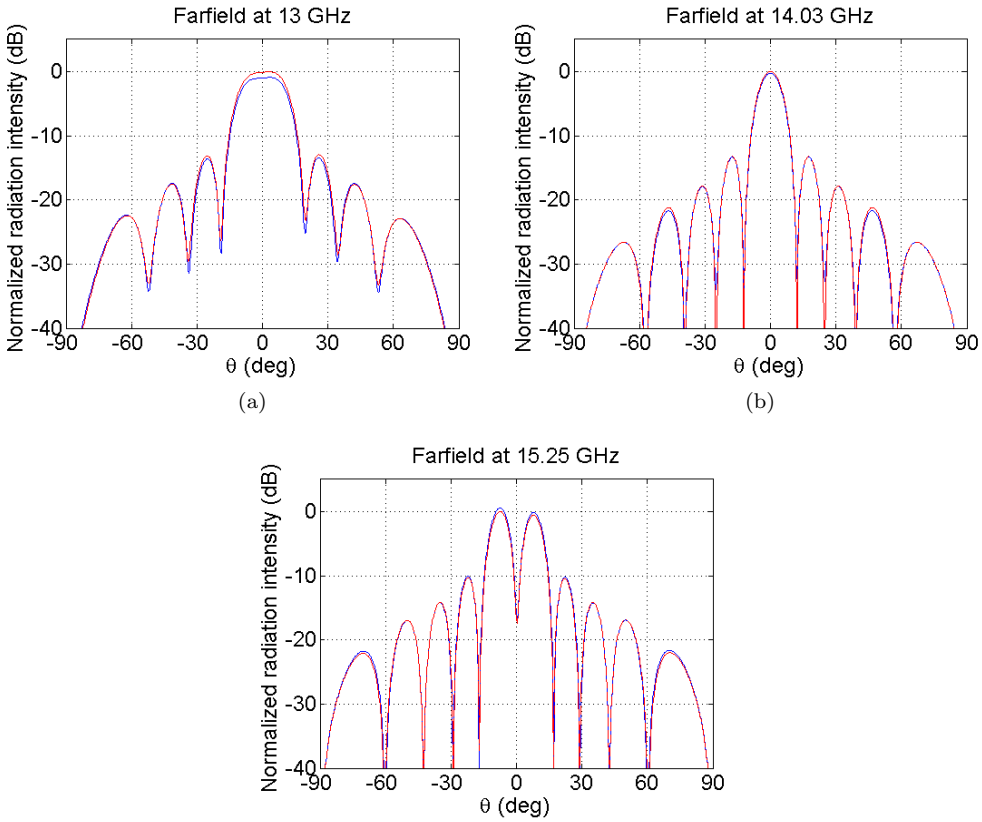

Figure 5.3: As Figure 5.2, but the case with mutual coupling is calculated both by our expressions (solid blue curves) and by Elliott's expressions (dashed blue curves, not well visible) for the mutual coupling.

First of all, the different curves are hard to distinguish. Secondly, we have normalized the cases with mutual coupling on the corresponding cases without mutual coupling. For these reasons, we recalculate the patterns at 9.41 GHz and normalize on a single maximum, namely the one of the array with varying offsets and without mutual coupling. Moreover, we focus on a limited sector of the patter from -15 to 15 degrees. Figure 5.10 shows the corresponding patterns. The squint of 5 degrees is clearly visible. Both for varying offsets and for uniform offsets we observe that mutual coupling has an enhancing effect of more than 1 dB. As explained in the previous section, this effect may be due to re-radiation of coupled power. We also observe a large difference of more than 10 dB between the cases with varying and uniform offsets. We will investigate this difference in more detail.

In our model one of the input parameters is V_1. This voltage is the mode voltage in the waveguide section containing slot 1, which is located next to the load. In our model V_1 is set to 1 V for all the test cases. We should however emphasize that V_1 is not directly linked to the mode voltage at the feed and, therewith, to the input power of the waveguide. To properly compare the cases with varying and uniform offsets we need to know the mode voltage at the slot next to the source, which is in this case V_{40}. To compute this voltage, we employ relation (4.38) give by

$$V_q = V_1 \Psi_q + jK_1 \sum_{p=1}^{q-1} f_p V_p^{\text{slot}} \sin((q-p)\theta). \tag{5.27}$$

This relation can be efficiently implemented using the results that are already obtained while

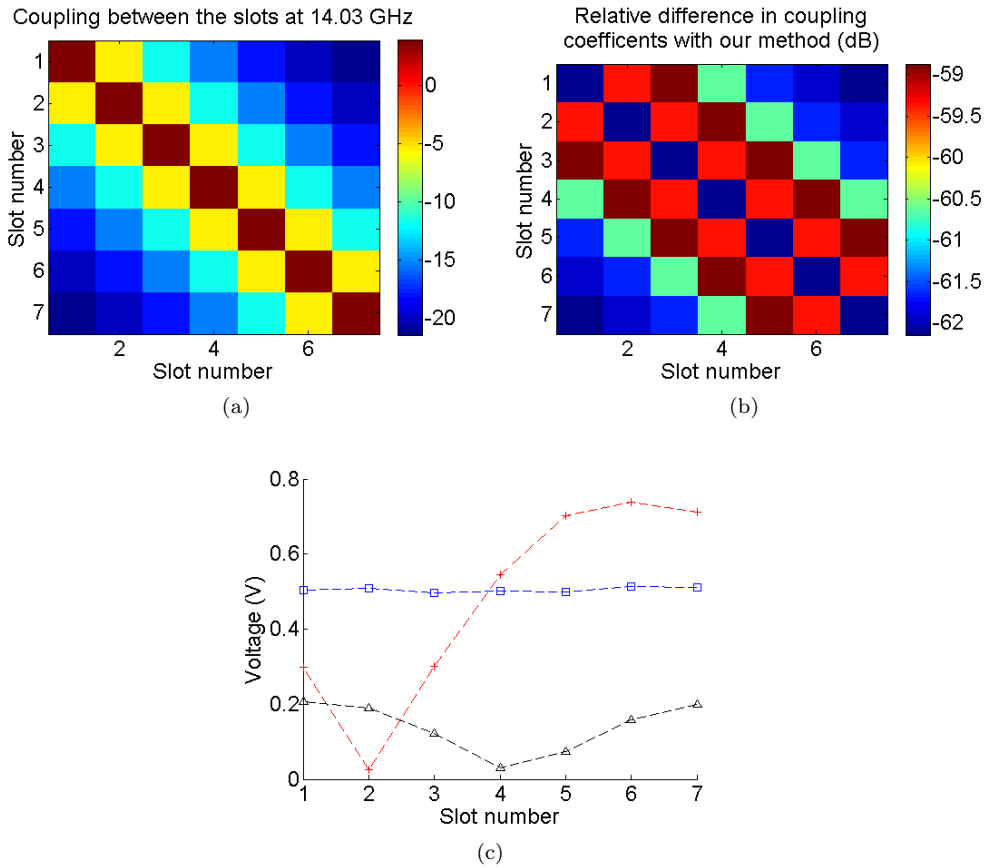

Figure 5.4: For the slotted waveguide array with parameters listed in Table 5.1: (a) the moment matrix for our mutual-coupling expressions, (b) the relative difference of the moment matrices obtained by Elliott's and our expressions, (c) slot voltages for the frequencies 13 Ghz (red, +), 14.03 GHz (blue, □) and, 15.25 (black, △).

computing the slot voltages. The vectors Ψ and V^{slot} are available after the computation of the slot voltages, and the parameter K_1 and the vector f can be extracted from the parameters used to compute the Ψ and V^{slot}.

The mode voltages V_{40} of the arrays shown in Figure 5.10 are presented in Table 5.3. Beside these voltages we have also computed the total power radiated by the arrays. To this end we have applied a 2D Simpson rule to (5.25). From the values in the table we observe that the mode voltages in the cases with varying slot offsets are about a factor 3 times greater than the mode voltages in the cases with uniform slot offsets. The result shows that we do not have equal input powers for the waveguides with varying and uniform offsets. The difference in the radiated power is more than a factor 10, which corresponds to the 10 dB difference in radiation intensity observed before.

To obtain comparable mode voltages at the feed, we could increase the voltage V_1. For the case with mutual coupling, Table 5.4 shows the mode voltages and the radiated powers for the array with uniform offsets at two values of V_1, namely $V_1 = 1$ and $V_1 = 3$ V. For comparison we have added the results of the array with varying offsets and $v_1 = 1$V. For $V_1 = 3$ V, the mode voltage at the feed of the array with uniform slot offsets is 5.17 V. This mode voltage is still lower than that of the array with varying offsets and, consequently, the radiated power is lower as well. We can further tune the voltage V_1 to obtain exactly the same mode voltage V_{40} as in the case with varying offsets. In this respect we note that from our matrix equation (4.47) and the relation

for the mode voltages (4.38), it follows that these voltages are linear in V_1. Thus to obtain the same mode voltage V_{40} we need to set V_1 to 5.36/5.17×3 V = 3.11 V. For this mode voltage at slot 40, the case with uniform offsets requires the same input power as the case with varying offsets, since in both cases slot 40 has exactly the same offset. The radiated power with uniform offsets is however still lower than with varying offsets. Given the quadratic relation between V_1 and the radiated power, we estimate the output power for uniform offsets, with V_1 = 3.11 V, at $(5.36/5.17)^2 \times 0.0104 = 0.0112$ W instead of 0.015 W for varying offsets. We thus conclude that the case with varying offsets results in a more efficient radiation.

Table 5.2: Parameters for an array of 40 slots

Variable	Value
Frequency	9.410 GHz
Number of slots	40
Slot spacing	0.029 m
Waveguide width (a)	0.0180 m
Waveguide height (b)	0.008 m
Offset from centre	varying
Slot length (2l)	0.015 m
Slot width (2w)	0.001 m
Thickness of the wall	0 m
Type	traveling-wave

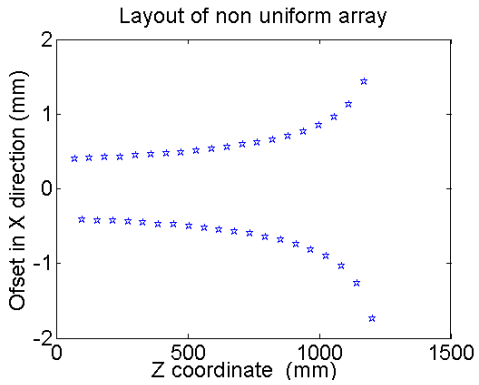

Figure 5.5: Layout of non uniform an array of 40 slots with the distance from the feed and the offset from the centre line as parameters.

Table 5.3: The mode voltages and the radiated powers of the slotted waveguides for which the patterns are shown in Figure 5.10.

Array	Mode voltage (V)	radiated power (W)
Non-varying offsets with mutual coupling	5.36	0.015
Non-varying offsets without mutual coupling	4.73	0.0109
varying offsets with mutual coupling	1.72	0.0011
varying offsets without mutual coupling	1.67	0.0009

From the two test cases can be concluded that our software computer the patterns accurately. However in the last example is shown that the radiated power and the input voltages need to be checked when using the code.

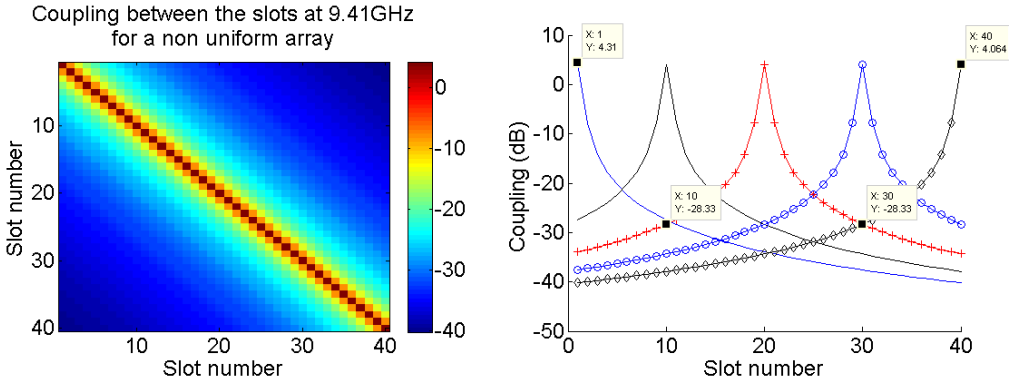

(a) (b)

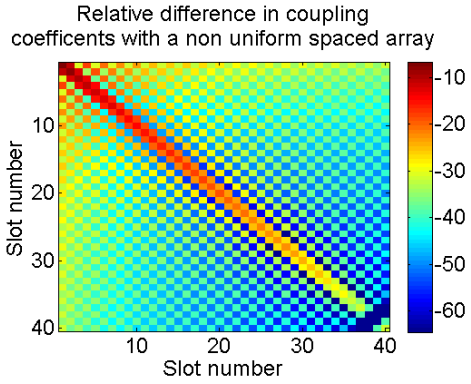

(c)

Figure 5.6: (a) Absolute values of the moment-matrix components of the waveguide with non-uniform slot offsets. (b) The coupling coefficients of slots 1, 10, 20, 30, and 40 as given by the corresponding columns in the moment matrix. (c) Relative differences of the moment-matrix components of the arrays with uniform and non-uniform offsets.

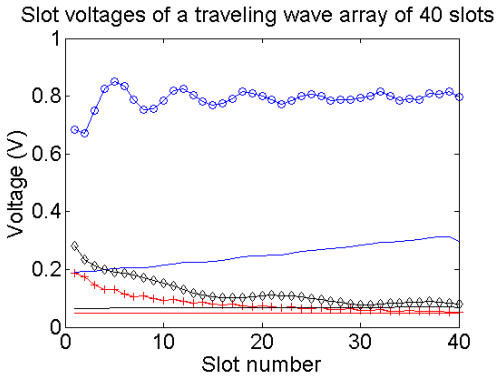

Figure 5.7: Slot voltages for an array of 40 slots at 9 GHz (red), 9.41 GHz (blue), and 10 GHz (black). Uniform offsets (no marker) versus varying offsets (with marker) for a traveling-wave array including mutual coupling. coupling is included.

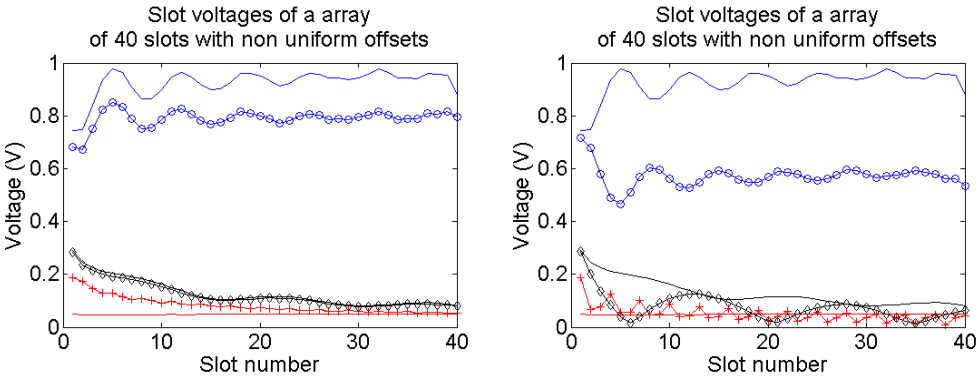

(a) (b)

Figure 5.8: Slot voltages for an array of 40 slots at 9 GHz (red), 9.41 GHz (blue), and 10 GHz (black). (a) With mutual coupling (no marker) versus without mutual coupling (marker) for a traveling-wave array with varying offsets. (b) Traveling-wave array (no marker) versus standing-wave array (marker) with varying offsets and mutual coupling is included.

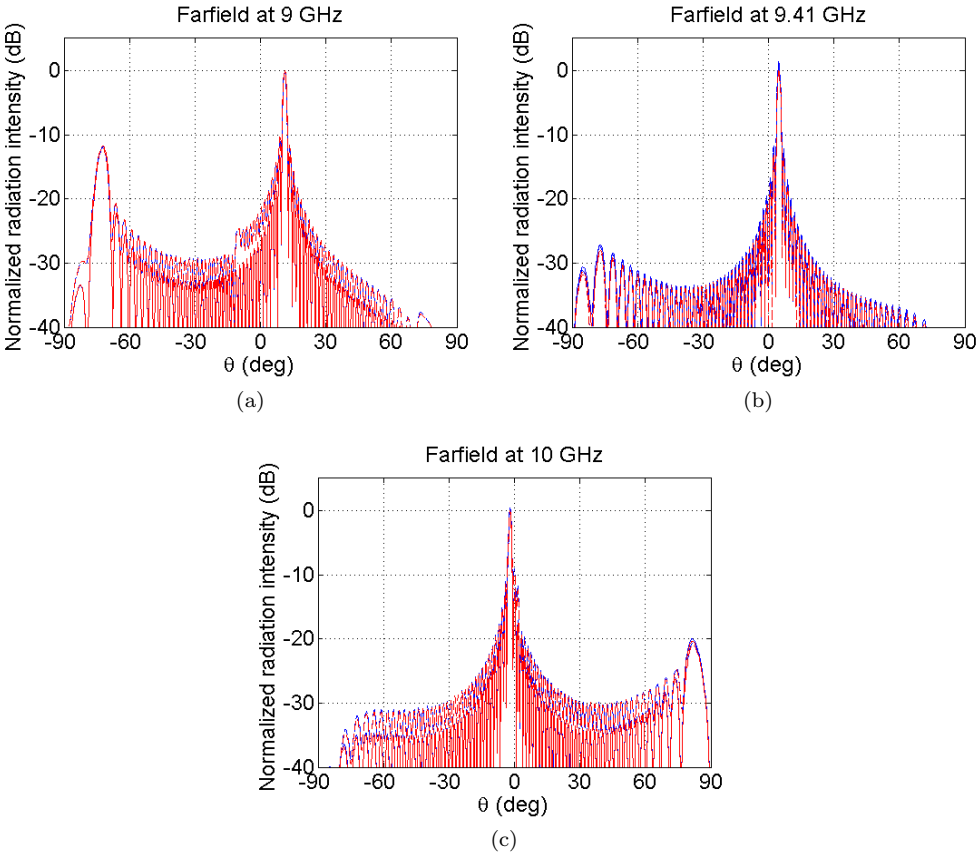

(a) (b) (c)

Figure 5.9: The far-field antenna patterns at 9 GHz (a), 9.41 GHz (b) and, 10 GHz (c) for an array of 40 slots with varying slot offsets (dashed) and uniform offsets (solid) for the cases with (blue) and without (red) mutual coupling. Normalization: Both for varying offsets and for uniform offsets, the normalization is the maximum of the case without mutual coupling.

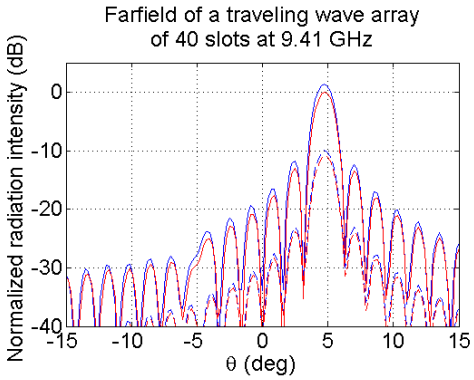

Figure 5.10: The far-field antenna patterns at 9.41 GHz for a traveling-wave array of 40 slots with uniform offsets(dashed) and with varying offsets (solid) for the cases with (blue) and without (red) mutual coupling. Normalization: All curves are normalized on the maximum of the case with varying offsets and without coupling.

Table 5.4: The mode voltages and the radiated powers for the slotted waveguides with mutual coupling as in Table 5.3 with increasing values of V_1 for the waveguides with varying offsets.

Array	V_1 (V)	Mode voltage V_{40} (V)	Radiated power (W)
Non-varying offsets	1	5.36	0.015
varying offsets	1	1.72	0.0011
varying offsets	3	5.17	0.0104

Chapter 6

Conclusions and Recommendations

In this chapter the conclusions and recommendations are going to be presented. The conclusion and the corresponding recommendations are going to be presented in the same order as they are addressed in this report. The recommendations for future work are going to be presented at the end of this chapter.

6.1 System

This thesis work assisted the design investigation project for TOFsat, a small FMCW synthetic aperture radar satellite for remote sensing and monitoring. Various system aspects where investigated for their impact on system disign and performance.

To investigate the feasibility of the system, the noise equivalent sigma zero has been investigated(NESZ), this can be found in Chapter 3.1. A NESZ of -18 dB at an incidence angle of 24° can be obtained with 100 W of transmit power, the effective aperture of the antenna can be about 3 m^2 or with 50 W of transmit power and about 6.25 m^2 antenna area.

The ambiguities in range have also been investigated. The effect of the ambiguous projections of the ground depends on the pattern of the used antenna. One of the ambiguous projections of interest is the nadir return. The methods to evaluate the ambiguities are presented in Chapter 3.2. The ambiguous projection of nadir return in the image can be avoided by changing the SRF.

Due to high demands on the isolation between the transmit chain and the receive chain a single antenna solution with continuous transmission turned out to be not possible. To avoid the problem of isolation, gated FMCW has been investigated. Due to the large swath, and consequently the low maximum gating frequency, in our application gated FMCW was not suitable. In the case with two antennas on one satellite the isolation between the two antennas needs to be about 100 dB, which is high on a small satellite. To ensure the isolation between the transmit chain and the receive chain a bi-static option with two satellites is considered. Only a bi-static option is considered feasible.

The antennas considered for the satellite are: a parabolic dish, a full phased array, a reflect array, and a slotted waveguide array. The options are extensively discussed in Chapter 3.4. Based on the high efficiency and relatively low weight the slotted waveguide array is the best option for our satellite.

For the downlink a commercial system is available, it weighs 6 kg and consumes 60 W. Such a solution is too heavy and consumes too much power for our small satellite. An alternative downlink system has been proposed with patch antennas. It is described in Chapter 3.5. The proposed alternative would consume less power and it weighs less than the commercially available system. Thus for the final satellite it is more efficient in power and weight to use a custom built downlink system.

6.2 The Slotted Waveguide Antenna

In the initial phase of the design the analysis of the far field antenna pattern was limited to a sinc^2 shape. For a more precise performance analysis of the satellite SAR, a fast code for accurate antenna pattern analysis is required. Within TNO there was a code available that is capable of calculating the far field pattern using the array factor for the geometry of a slotted waveguide. This code doesn't take the mutual coupling into account. To perform a better evaluation of the waveguide array the far field pattern considering the mutual coupling of the slotted waveguide antenna needs to be obtained.

From literature expressions for a linear system have been derived to obtain the slot voltages as in Chapter 4. In the model the following assumptions have been made:

- The expressions derived use only a propagating TE_{10} mode, the higher order modes are neglected.
- The electric field is assumed to be directed perpendicular to the long side of the slot.
- In the slot the field is assumed to be symmetrical and uniform in the z direction of the slot.

The expressions in this work result in a linear system that describes a slotted waveguide array.

The obtained linear system has a coupling matrix with the mutual coupling coefficients and separately obtained self coupling coefficients. The expressions of Yee for the self coupling did not converge, in this work they have been modified and corrected as described in Chapter 4.3.4. The self coupling expressions have been compared with examples in literature. The code presents comparable results with the measured values for the self coupling.

In the original expressions of Elliott the mutual coupling is calculated using a double integral. In our work the integrals have been split up in two separate integrals and implemented using numerical approximation of the integrals. Both methods have been implemented and the differences are small, thus the faster code using the two integrals can be used.

A code has been generated to obtain the far field radiation pattern from the slot voltages. The far field patterns obtained are validated for a slotted waveguide array of 7 slots and a slotted waveguide array of 40 slots. From the simulations we found that the mutual coupling also can have constructive behaviour.

For the array with 40 slots both travelling wave excitation and standing wave excitation have been analysed. The standing wave case showed a lot less radiated power for this geometry. With the same input parameters the mode voltages at the input, i.e. the section containing the first slot, where considerably different for both cases. In the code the mode voltage at the last section of the waveguide has to be provided and not the mode voltage at the input. A considerable difference was found between the input voltages for the travelling wave case and the standing wave case. Even with the same input mode voltages the radiated powers where not the same.

6.3 Recommendations

In evaluation of the NESZ for the different antenna options, the calculation of the normalised radiation pattern of a parabolic reflector is quite computationally intensive. The code used for this calculation originates from Balanis, the integration used is not cascaded, a custom made code might speed up the process. Another way to speed up the calculation of the process is to limit the number of points that is evaluated for the antennas. The range ambiguities only evaluate the first ambiguous projection on both sides of the swath. The maximum and minimum angle evaluated can be lowered to only accommodate the swath and the adjacent ambiguous projections. However if the maximum and minimum angle are lowered the nadir return has to be evaluated separately.

The code that calculates the range ambiguity ratio only evaluates the first ambiguous projections before and after the swath. This could be extended with a test that calculates the location of the nadir return to avoid separate evaluation of this projection.

The proposed system for the downlink shows considerable improvements on power consumption. The calculations are made with the same components for the amplification chain as in the radar system. For more precise calculations the carrier frequency needs to be selected and the available bandwidth needs to be specified.

The evaluation of the waveguide is done under the assumption that only the TE_{10} mode propagates. In our case this assumption is valid since the dimensions of the waveguide are chosen in such a way that only the TE_{10} mode propagates. However if the waveguide dimensions change the higher order modes might also play a role, and the model might be extended to also involve the higher order modes.

In the geometry the waveguide is aligned parallel to the azimuth direction of the radar. The model derived only represents the far field radiation intensity of one slotted waveguide array. In the satellite configuration multiple arrays are placed parallel to the azimuth direction and multiple waveguides are stacked in elevation direction. The effects of this arrangement can be modelled using a standard array factor implementation for (scanning) arrays. However the standard array factor does not account for the coupling between the separate waveguides. The effects of this coupling between the slotted waveguides should be modelled in a 2D model.

Finally the model of the waveguide should be used with the real parameters of the waveguide that is going to be used in the satellite.

Appendix A

Maxwell's Equations

In this appendix, we consider the electromagnetic field in free space generated by time-harmonic electric and magnetic current densities $\mathscr{J}$ and $\mathscr{M}$ with radian frequency ω. The field is governed by Maxwell's equations,

$$\operatorname{curl}\mathscr{E} = -\frac{\partial\mathscr{B}}{\partial t} - \mathscr{M} \qquad \operatorname{curl}\mathscr{H} = \frac{\partial\mathscr{D}}{\partial t} + \mathscr{J} \tag{A.1}$$

Here, $\mathscr{E}$ and $\mathscr{H}$ are the strengths of the electric and magnetic field, $\mathscr{D}$ and $\mathscr{B}$ are the densities of the electric and magnetic flux, and t is the time variable. The conservation of electric and magnetic charges are described by the continuity equations

$$\frac{\partial\varrho_e}{\partial t} + \operatorname{div}\mathscr{J} = 0 \qquad \frac{\partial\varrho_m}{\partial t} + \operatorname{div}\mathscr{M} = 0 \tag{A.2}$$

where ϱ_e and ϱ_m are the electric and magnetic charge densities. The constitutive behavior of free space is described by

$$\mathscr{B} = \mu_0\mathscr{H}\,, \qquad \mathscr{D} = \varepsilon_0\mathscr{E} \tag{A.3}$$

where ε_0 and μ_0 are the permittivity and the permeability of free space. Their values are $\mu_0 = 4\pi\cdot 10^{-7}\,\mathrm{V\,s/A\,m}$ and $\varepsilon_0 = 1/\mu_0 c_0^2$, where $c_0 = 2.99792458\cdot 10^8\,\mathrm{m/s}$ is the free-space velocity of light. The time-harmonic behavior of the electric current density is modeled as

$$\mathscr{J}(\boldsymbol{x},t) = \operatorname{Re}\left(\boldsymbol{J}(\boldsymbol{x})\,e^{j\omega t}\right) = \frac{1}{2}\left[\boldsymbol{J}(\boldsymbol{x})\,e^{j\omega t} + \boldsymbol{J}^*(\boldsymbol{x})\,e^{-j\omega t}\right] \tag{A.4}$$

where $*$ indicates the complex conjugate and $\boldsymbol{x}$ represents the position. The time-harmonic behavior of the magnetic current density is modeled analogously with magnetic current $\boldsymbol{M}(\boldsymbol{x})$. Incorporating the time-harmonic behavior and the constitutive behavior in Maxwell's equations and continuity equations, we arrive at

$$\operatorname{curl}\boldsymbol{E} = -j\omega\mu_0\boldsymbol{H} - \boldsymbol{M} \qquad \operatorname{curl}\boldsymbol{H} = j\omega\varepsilon_0\boldsymbol{E} + \boldsymbol{J} \tag{A.5}$$

$$j\omega\rho_e + \operatorname{div}\boldsymbol{J} = 0 \qquad j\omega\rho_m + \operatorname{div}\boldsymbol{M} = 0 \tag{A.6}$$

From (A.5), we find $\operatorname{div}\boldsymbol{H} = \rho_m/\mu_0$ and $\operatorname{div}\boldsymbol{E} = \rho_e/\varepsilon_0$. In our analysis we will mainly deal with cases in which the electric (volume) current $\boldsymbol{J}$ and the electric charge ρ_e are zero. Consequently, $\operatorname{div}\boldsymbol{E} = 0$, i.e., the electric field is solenoidal.

Bibliography

[1] M. Eineder. Terrasar-x ground segment basic product specification document. Technical report, DLR, 2006.

[2] DLR. Presentation. ESA workshop polinsar 2003.

[3] U. Naftaly Y. Sharay. Tecsar: design considerations and programme status. In *Radar Sonar Navig., Vol. 153.*

[4] J.C. Curlander and R.N. McDonough. *Synthetic Aperture Radar: Systems and Signal Processing.* Wiley Series in Remote Sensing. Wiley, 1991.

[5] G. Rees. *Physical Principles of Remote Sensing.* Physical Principles of Remote Sensing. Cambridge University Press, 2001.

[6] P.Hoogeboom. Lecture slides l 8. Lectures RRSEA, 5 2010.

[7] A. Meta. *Signal processing of FMCW Synthetic Aperture Radar data.* PhD thesis, Tu delft, 2006.

[8] *First demonstration of an X-band FMCW SAR*, 2005.

[9] TNO. Minisar. Technical report, TNO.

[10] J.J.M. de Wit and P. Hoogeboom. Sar: A novel application for fm-cw radars. In *Microwave Conference, 2001. 31st European*, pages 1 –4, sept. 2001.

[11] Matern Otten. Signaal-ruisverhoudingen in sar. Technical report, TNO, 8 2000.

[12] M.W. Spencer and D.G. Long. Characterization of global near-nadir backscatter for remote sensing radar design. In *Geoscience and Remote Sensing Symposium, 1999. IGARSS '99 Proceedings. IEEE 1999 International*, volume 1, pages 440 –442 vol.1, 1999.

[13] S.-E. Hamran, T. Berger, L. Hanssen, and M.J. Oyan. Gated fmcw sar system. In *Radar Conference, 2008. EuRAD 2008. European*, pages 487 –490, oct. 2008.

[14] Y. Sharay and U. Naftaly. Tecsar: design considerations and programme status. *Radar, Sonar and Navigation, IEE Proceedings* -, 153(2):117 –121, april 2006.

[15] Constantine A Balanis. *Antenna theory : analysis and design.* Hoboken, NJ : John Wiley, 2005.

[16] C. Han, J. Huang, and Kai Chang. Cassegrain offset subreflector-fed x/ka dual-band reflectarray with thin membranes. *Antennas and Propagation, IEEE Transactions on*, 54(10):2838 –2844, oct. 2006.

[17] P. James and S.J. Vetterlein. A wideband resonant slotted waveguide array for space sar applications. In *Antennas and Propagation, 1999. IEE National Conference on.*, pages 279 –282, 1 1999-march 31 1999.

[18] R. Kwok and W. T. K. Johnson. Block adaptive quantization of Magellan SAR data. *IEEE Transactions on Geoscience and Remote Sensing*, 27:375–383, July 1989.

[19] SSTL, http://www.sstl.co.uk/Downloads/Datasheets/Subsys-datasheets/Antenna-Pointing-Mechanism-ST0118003-v002-00. *X-Band Downlink Suite*.

[20] Louis J. Ippolito. *Satellite communications systems engineering*. Wiley, 2008.

[21] J.H. Weber. Tabels:required eb/n0 (in db) for msk, mpsk, and mfsk. Technical report, TU Delft, 8 2010.

[22] A.A. Oliner. The impedance properties of narrow radiating slots in the broad face of rectangular waveguide, part i. *Antennas and Propagation, IEEE Transactions on*, AP-5:4 – 11, 1957.

[23] A.A. Oliner. The impedance properties of narrow radiating slots in the broad face of rectangular waveguide, part ii. *Antennas and Propagation, IEEE Transactions on*, AP-5:12 – 20, 1957.

[24] Hung Yee. Impedance of a narrow longitudinal shunt slot in a slotted waveguide array. *Antennas and Propagation, IEEE Transactions on*, 22(4):589 – 592, jul 1974.

[25] D.J. Bekers. Modeling and analysis of waveguide arrays with longitudinal slots. Technical report, TNO The Hague, Techical Note, 2012.

[26] R. Elliott. An improved design procedure for small arrays of shunt slots. *Antennas and Propagation, IEEE Transactions on*, 31(1):48 – 53, jan 1983.

[27] R.S. Elliott. *Antenna theory and design*. Prentice-Hall, 1981.

[28] R. Elliott and W. O'Loughlin. The design of slot arrays including internal mutual coupling. *Antennas and Propagation, IEEE Transactions on*, 34(9):1149 – 1154, sep 1986.

[29] S.R. Rengarajan. Compound radiating slots in a broad wall of a rectangular waveguide. *Antennas and Propagation, IEEE Transactions on*, 37(9):1116 –1123, sep 1989.

[30] M. Hamadallah. Frequency limitations on broad-band performance of shunt slot arrays. *Antennas and Propagation, IEEE Transactions on*, 37(7):817 –823, jul 1989.

[31] D.J. Bekers. *Finite Antenna Arrays, An Eigencurrent Approach*. PhD thesis, TUE, 2004.